Mechanical Systems and Signal Processing 146 (2021) 107003

Contents lists available at ScienceDirect

Mechanical Systems and Signal Processing

journal homepage: www.elsevier.com/locate/ymssp

Mechanical systems virtual sensing by proportional observer and multi-resolution analysis

Francesco Saltari [a], Daniele Dessi [b,*], Franco Mastroddi [a]

[a] University of Rome "La Sapienza" Dept. of Mechanical and Aerospace Engineering, Via Eudossiana 18, 00184 Rome Italy
[b] CNR-INM Institute of Marine Engineering – National Research Council, Via di Vallerano 139, 00128 Rome Italy

ARTICLE INFO

Article history:
Received 13 December 2019
Received in revised form 9 April 2020
Accepted 23 May 2020

Keywords:
Virtual Sensing
Multi-Resolution Analysis
State estimation
Spectral methods
Structural dynamics

ABSTRACT

A technique to reconstruct the displacement field throughout the structure from pointwise measurements under different noise sources is proposed. The developed estimator is a Proportional Observer (PO) that exploits a linear, frequency independent, relation between the estimated state-space vector and the measurements. To improve its accuracy, the PO concept is then extended to the definition of a sequence of proportional observers, each one acting on a signal decomposition provided by wavelet multi-resolution analysis, or a Multi-Resolution Proportional Observer (MR-PO). The considered numerical test case is a straight, uniform beam with an unmodeled stiffness reduction provided by a notch, which allows for characterizing analytically this model uncertainty. The input data is given by virtual strain measurements collected on the top face of the beam, whereas the estimated state variables are the time dependent coordinates of the modal expansion of the vertical displacement along the beam elastic axis. An optimization solver, which minimizes the estimation error, is employed to get the gain matrix of the proposed observers. The effect of different noise sources, like process and measurement noise and unknown excitation, on the estimation accuracy is taken into account with a sensitivity analysis. The obtained results assess the effectiveness of the combination between the PO concept and wavelet multi-resolution analysis as a tool for developing digital twin models based on experimental data.

1. Introduction

The availability of high-performance computing at different scales makes nowadays the implementation of digital twins of complex structural systems a not so far objective. Reproducing the behaviour of such systems requires high-fidelity models which need to be trained with the sensor data from the structure itself to increase the accuracy. In principle, a digital twin can represent the system in an accurate way throughout its operational life with the desired time and spatial resolution, provided that environmental and loading conditions as well as ageing factors, are correctly described. For certain purposes, like structural health monitoring, the full-field description of continuous systems can be also achieved with a virtual sensing approach which brings the sensor data at the centre of the reconstruction technique. Indeed, virtual sensing aims at providing a reliable estimation of a physical variable that is not possible to measure directly. As there is no limitation in the number of virtual sensors, virtual sensing seeks to reconstruct the entire field of the selected variables for continuous systems.

* Corresponding author.
E-mail address: daniele.dessi@cnr.it (D. Dessi).

https://doi.org/10.1016/j.ymssp.2020.107003
0888-3270/

Post-processing of data can be also embedded in the numerical process to get quantities that are unmeasurable by definition, extending the capability of virtual sensors.

Typically, the problem of virtual sensing of structures has been addressed in different ways. In structural engineering, following the pioneer work carried out by Maniatty et al. [1], a more systematic approach to the problem of determining in real-time the applied loads, stresses, and displacements motivated the development of the inverse finite element method (iFEM) at NASA Langley [2], successively consolidated by Tessler et al. [3]. The use of sub-structuring techniques (see [4,5]) has been also successively employed to obtain the reconstruction of the displacement field. More general approaches not necessarily limited to identify structural variables, have been typically considered in control theory applications, for instance through modal filters as in [6–8]. Restricting to recent years, Hwang et al. [9] proposed the use of Kalman filter to estimate the modal elastic deflections. The unknown state-space vector was made up by modal coordinates and velocities relative to a numerical model of a building; once estimated on the basis of virtual measurements, the modal coordinates allowed for providing the correspondent wind loads. Similarly, Papadimitriou et al. [10] successfully predicted the fatigue-life reduction of metallic structures by using the stress field obtained by means of Kalman filter. Lourens et al. [11] introduced the so-called augmented Kalman filter, which adds the unknown external forces to the state-space vector to be estimated. From the dynamic modelling point of view, these external forces, though unknown, were provided as the result of a random walk dynamics with an associated process noise. Continuing the work of Gillins and De Moor [12], Lourens et al. [13] proposed a new technique to obtain a joint estimation of the state-space variables (made up by modal coordinates and velocities) as well as of the input. The joint input-response estimation exploits an algorithm similar to Kalman filter that, besides the usual tasks of measurement update and time update, considers a further step concerning the input estimation, recursively estimated by means of an unbiased minimum-variance process. More recently, Naets et al. [14] proposed to exploit the augmented Kalman filter to get an estimation of variation of system parameters along with system response and unknown external forces.

Despite of their ability to track unmeasured time-histories, all the methods that exploit Kalman filtering are not natural for second-order structural systems as highlighted by Balas [15]; the time derivative of the estimated modal coordinate (*e.g.*, relative to displacements) is not equal to the estimated velocity. This limit is magnified when unknown external forces are dominant with respect to the process and measurement noises, and consequently Balas [15] proposed a first-order observer aimed to reduce the gap, following previous attempts to adapt the Kalman filter formulation to second-order systems by Hashemipour and Laub [16] and Belvin [17]. More recently, Demetriou [18] presented a natural second-order observer that utilizes a parameter-dependent Lyapunov function to ensure the asymptotic convergence of the error on the state-space variables. Demetriou [19] also adapted the observer formulation for second-order systems with an unknown input to detect faults of mechanical systems. Among approaches based on second order observers, Hernandez [21–23] addressed the problem of finding the optimal observer gain by minimizing the estimation error in the frequency domain, although the observation process is naturally defined in time domain. The statistics of the noise and external loads are expressed by means of power spectral densities instead of the covariance matrices typically used in Kalman filter. This enhances the capability of observing linear (structural) systems that are intrinsically featured by their frequency domain behavior.

In this paper, in the perspective to introduce improvements in observer-based virtual sensing techniques for structural problems, an observer exploiting a linear, frequency independent, relation between the estimated state-space vector and the measurement vector is introduced, named in the following as Proportional Observer (PO). This approach is then generalized to the definition of a sequence of proportional observers, each one acting on a signal decomposition provided by wavelet multi-resolution analysis, named as Multi-Resolution Proportional Observer (MR-PO). The PO shares the same form with modal filters, but unlike the latter it takes into account the model structural features as well as excitation and noise statistics in building the error function; the availability of such analytical expression speeds up the error computation, and is a key point for employing error minimization procedures when dealing with large systems.

As a second point, to increase the level of confidence in using these numerical tools before real-life applications (*e.g.*, see Ref. [24]), the reconstruction of the elastic deflection field is carried out on a simple and analytically modelled case study, *i.e.*, a straight beam on spring foundations. The uniform beam is provided with a small stepwise variation of the cross section, namely a notch, which introduces a modelling uncertainty in the mass and stiffness distributions. Virtual sensors are provided by strain gages applied on the beam from which the entire displacement field is reconstructed. Then, in order to keep the number of state variables low, the modal coordinates associated to a limited number of beam modes have been considered, as typical in many virtual sensing approaches related to structural variables.

To compare the performance of these techniques against existing methods, the Modal Based Observer (MBO) proposed by Hernandez [21] is also applied to the present case. Even if the PO, and consequently the MR-PO, can be developed apart from MBO, in this paper we will show that, if modal displacements are the target of the reconstruction process and certain conditions are satisfied, the MBO takes the form of the proposed observer. This feature, as well as other similarities in the analytical and numerical development, suggests denoting the proposed approaches as 'observers'.

The observer synthesis, in all the considered methods, is then based on selecting the coefficients of a gain matrix via an optimization procedure, which aims to minimize the power spectral density (or the covariance) of the estimation error, defined as the difference between the estimated and the true state-space vector. The optimization process does not require to compare, at each iteration, the new predicted time-histories with the true solution to evaluate the error function. Throughout the paper, analytical expressions of the error function are derived and minimized by a proper choice of the observer gain. These analytical expressions include the different noise sources affecting the system response and the measurements, whose statistical modelling is required to fully characterize the error. In this way, the estimation sensitivity on

the measurement and process noise is efficiently carried out, and the effectiveness of the optimization process can be easily assessed under different conditions.

The paper is organized as follows. The dynamical model of the considered mechanical system is presented in Section 2 along with a generalized formulation of the MBO which allows for introducing the basic elements of the observation process. Section 3 introduces the Proportional Observer and the Multi-Resolution Proportional Observer as well as the correspondent analytical formulations of the estimation error. The simple structure to which the considered methods are applied is described in Section 4 and the optimization procedure to calculate the observer gain is explained in Section 5. The numerical results accounting for the capability of the methods to approximate the true solution based on virtual strain measurements are finally discussed in Section 6.

2. Mechanical system modelling and its model-based observer

In the present paper, we shall limit our attention to linear mechanical systems which can be represented in time domain, including suitable initial conditions as:

$$\mathsf{M}\ddot{\mathsf{q}} + \mathsf{D}\dot{\mathsf{q}} + \mathsf{K}\mathsf{q} = \mathsf{f} + \mathsf{w} \tag{1}$$

where $\mathsf{q} \in \mathbb{R}^N$ is a vector of generalized coordinates (nodal displacements and rotations in finite element discretization or modal amplitudes), M, D and K denote the mass, damping and stiffness $N \times N$ matrices, respectively, $\mathsf{f} \in \mathbb{R}^N$ is the external force vector and the vector $\mathsf{w} \in \mathbb{R}^N$ accounts for modelling errors in terms of process noise. The system observations are assumed to be of the form:

$$\mathsf{y} = \mathsf{S}\mathsf{q} + \mathsf{v} \tag{2}$$

where the $M \times N$ matrix S relates linearly and instantaneously the measurement vector $\mathsf{y} \in \mathbb{R}^M$ to the vector of generalized coordinates q and $\mathsf{v} \in \mathbb{R}^M$ is the measurement noise vector. More general forms of Eq. (2) have been proposed but we limit ourselves to measurements expressed in terms of displacements like strain measurements. For linear systems, it is common to consider the Fourier transform of Eqs. (1) and (2), *i.e.*,

$$-\omega^2\mathsf{M}\tilde{\mathsf{q}} + i\omega\mathsf{D}\tilde{\mathsf{q}} + \mathsf{K}\tilde{\mathsf{q}} = \tilde{\mathsf{f}}(\omega) + \tilde{\mathsf{w}}(\omega) \tag{3}$$

$$\tilde{\mathsf{y}} = \mathsf{S}\tilde{\mathsf{q}} + \tilde{\mathsf{v}}(\omega) \tag{4}$$

where $\sim$ indicates the transformed variables and the dependence on frequency ω is highlighted only in the case of external input and noise. The frequency response function matrix $\mathsf{H}(\omega)$ for the mechanical system alone is given by:

$$\mathsf{H}(\omega) = \left[-\omega^2\mathsf{M} + i\omega\mathsf{D} + \mathsf{K}\right]^{-1} \tag{5}$$

relating the state-space vector to the inputs, *i.e.*, $\tilde{\mathsf{q}} = \mathsf{H}(\omega)\left(\tilde{\mathsf{f}}(\omega) + \tilde{\mathsf{w}}(\omega)\right)$.

2.1. Model-based observer

For the mechanical system defined by Eq. (1), suitable natural observers have been proposed in the past literature (see Refs. [17–23]). Here, we specifically consider the Model-Based Observer introduced by Hernandez [21] as it is the starting point for the proposed theoretical developments. Thus, the MBO theory is recalled and generalized in this paper which allows us to introduce several definitions later included in the development of the proposed methods as well. The equations of linear second-order observer concerning the system modelled by Eq. (1) can be generally expressed as follows:

$$\mathsf{M}\ddot{\hat{\mathsf{q}}} + \mathsf{D}\dot{\hat{\mathsf{q}}} + \mathsf{K}\hat{\mathsf{q}} = \mathsf{L}(\mathsf{y} - \mathsf{S}\hat{\mathsf{q}}) \tag{6}$$

where the symbol $\hat{}$ indicates the estimated variable (in this case, the estimated state-space vector $\hat{\mathsf{q}}$) and L is the observer $M \times N$ gain matrix. Eq. (6) represents the mathematical model of the feedback control system. By defining the estimation error $\mathsf{e} \in \mathbb{R}^N$,

$$\mathsf{e} = \mathsf{q} - \hat{\mathsf{q}} \tag{7}$$

and making use of Eqs. (1) and (6), one obtains the error dynamics as:

$$\mathsf{M}\ddot{\mathsf{e}} + \mathsf{D}\dot{\mathsf{e}} + \mathsf{K}\mathsf{e} + \mathsf{L}\mathsf{S}\mathsf{e} = \mathsf{f} + \mathsf{w} - \mathsf{L}\mathsf{v} \tag{8}$$

The Fourier transform of Eq. (8) yields:

$$\left[-\omega^2\mathsf{M} + i\omega\mathsf{D} + \mathsf{K} + \mathsf{L}\mathsf{S}\right]\tilde{\mathsf{e}}(\omega) = \tilde{\mathsf{f}}(\omega) + \tilde{\mathsf{w}}(\omega) - \mathsf{L}\tilde{\mathsf{v}}(\omega) \tag{9}$$

It is possible to introduce a transfer function H_e which expresses the dependence of the estimation error e on the inputs:

$$\mathsf{H}_e(\omega) = \left[-\omega^2\mathsf{M} + i\omega\mathsf{D} + \mathsf{K} + \mathsf{L}\mathsf{S}\right]^{-1}, \tag{10}$$

and consequently Eq. (9) provides its frequency response as:

$$\tilde{\mathrm{e}} = \mathrm{H}_e(\omega)\left(\tilde{\mathrm{f}} + \tilde{\mathrm{w}} - \mathrm{L}\tilde{\mathrm{v}}\right). \tag{11}$$

In the frequency domain, the closed-loop frequency response function H_O of the observer, relating the estimated state $\tilde{\hat{\mathrm{q}}}$ to the reference $\tilde{\mathrm{y}}$, can be generally expressed:

$$\mathrm{H}_O(\omega) = \left(\mathrm{H}^{-1} + \mathrm{LS}\right)^{-1}\mathrm{L} \tag{12}$$

such that:

$$\tilde{\hat{\mathrm{q}}} = \mathrm{H}_O(\omega)\tilde{\mathrm{y}}. \tag{13}$$

Moreover, recalling Eq. (4), one obtains:

$$\tilde{\hat{\mathrm{q}}} = \mathrm{H}_O\mathrm{S}\tilde{\mathrm{q}} + \mathrm{H}_O\tilde{\mathrm{v}}. \tag{14}$$

If the statistical features of the forcing terms in Eq. (11) as well as of the process and measurement noises are stochastic and uncorrelated to each other, the stable error response to the stochastic inputs is obtained as follows:

$$\Phi_{\mathrm{ee}}(\omega;\mathrm{L}) = \mathrm{H}_{\mathrm{e}}^{*}(\omega;\mathrm{L})\left(\Phi_{\mathrm{ff}}(\omega) + \Phi_{\mathrm{ww}}(\omega) + \mathrm{L}\Phi_{\mathrm{vv}}(\omega)\mathrm{L}^{\mathsf{T}}\right)\mathrm{H}_{\mathrm{e}}^{\mathsf{T}}(\omega;\mathrm{L}) \tag{15}$$

where $\Phi_{\mathrm{ee}}(\omega;\mathrm{L}), \Phi_{\mathrm{ff}}(\omega), \Phi_{\mathrm{vv}}(\omega)$ and $\Phi_{\mathrm{ww}}(\omega)$ indicate the power spectral density matrices. For the sake of clarity, the dependence on the gain L of the different terms is highlighted in the equation. Finally, Eq. (15) yields the covariances of the state error e as:

$$\left[\sigma_{\mathrm{ee}}^2\right] = \int_{-\infty}^{+\infty} \Phi_{\mathrm{ee}}(\omega;\mathrm{L})d\omega. \tag{16}$$

It is worth noting that the covariance matrix depends on the gain matrix L through Eq. (15). Thus, the aim is to minimize the trace of covariance in Eq. (16) by searching for the optimal matrix L once the noise and force statistics are established. This optimal gain can be analytically determined only for simple problems as done by Hernandez (Ref. [22]). In general cases, we need to rely on numerical approaches like the optimization procedure introduced later in Section 5.

3. Proposed estimators based on Proportional Observer concept

Recalling Eq. (15), it emerges how the gain L plays a central role in minimizing the estimation error on the system state-space vector q at two different levels: (*i*) adjusting the second-order observer to wipe out the disturbances and (*ii*) tuning the balance between the unknown inputs and the measurement noise. This complex functional dependence of the error on the gain matrix L is likely to provide optimal solutions that correspond only to local minima and consequently there is no guarantee that an absolute minimum is determined. To avoid this limitation, an alternate approach based on the Proportional Observer concept is hereafter introduced.

3.1. Single-resolution PO

The simplest form of the Proportional Observer can be formulated as follows:

$$\hat{\mathrm{q}} = \mathrm{Q}\mathrm{y}, \tag{17}$$

where Q is a $N \times M$ matrix of constant coefficients. Substituting the previous definition (Eq. (17)) into the error definition (Eq. (7)), one has:

$$\mathrm{e} = (\mathrm{I} - \mathrm{QS})\mathrm{q} - \mathrm{Q}\mathrm{v}, \tag{18}$$

or, equivalently, $\tilde{\mathrm{e}} = (\mathrm{I} - \mathrm{QS})\tilde{\mathrm{q}} - \mathrm{Q}\tilde{\mathrm{v}}$ in the frequency domain. Recalling that $\tilde{\mathrm{q}} = \mathrm{H}(\omega)\left(\tilde{\mathrm{f}} + \tilde{\mathrm{w}}\right)$, after substitution in the latter expression, it yields:

$$\tilde{\mathrm{e}} = (\mathrm{I} - \mathrm{QS})\mathrm{H}(\omega)\left(\tilde{\mathrm{f}} + \tilde{\mathrm{w}}\right) - \mathrm{Q}\tilde{\mathrm{v}}, \tag{19}$$

According to Eq. (19), the error is given by two contributions, one depending on the unknown inputs $\tilde{\mathrm{f}}$ and $\tilde{\mathrm{w}}$ and the other on the measurement noise $\tilde{\mathrm{v}}$, via different frequency response functions, respectively. Thus, the power spectral density of the error $\Phi_{\mathrm{ee}}(\omega)$ is related to the power spectral density of the inputs as:

$$\Phi_{\mathrm{ee}}(\omega;\mathrm{Q}) = (\mathrm{I} - \mathrm{QS})\,\mathrm{H}^{*}(\omega)[\Phi_{\mathrm{ff}}(\omega) + \Phi_{\mathrm{ww}}(\omega)]\mathrm{H}(\omega)^{\mathsf{T}}\,(\mathrm{I} - \mathrm{QS})^{\mathsf{T}} + \mathrm{Q}\,\Phi_{\mathrm{vv}}(\omega)\,\mathrm{Q}^{\mathsf{T}} \tag{20}$$

From Eq. (20), it is evident that the optimum choice of Q must be a trade-off between reducing the effect of the unknown inputs, so implying a low gain, and the effect of the measurement noise, requiring a high gain instead. It is worth noting that the first term on the r.h.s. of Eq. (20) contains implicitly the PSD of the state-space vector q. Thus, introducing the PSD of the state-space vector, *i.e.*,

$$\Phi_{qq}(\omega) = H^{*}(\omega)(\Phi_{ff}(\omega) + \Phi_{ww}(\omega))H(\omega)^{T}, \tag{21}$$

Eq. (20) is rewritten as:

$$\Phi_{ee}(\omega; Q) = (I - QS)\,\Phi_{qq}(\omega)\,(I - QS)^{T} + Q\,\Phi_{vv}(\omega)\,Q^{T}. \tag{22}$$

From the previous equation, the error variance matrix $\left[\sigma^2_{ee}\right]$ can be obtained as:

$$\left[\sigma^2_{ee}\right] = (I - QS)\left[\sigma^2_{qq}\right](I - QS)^{T} + Q\left[\sigma^2_{vv}\right]Q^{T} \tag{23}$$

where $\left[\sigma^2_{qq}\right]$ is the covariance associated to the modal coordinates that is defined as:

$$\left[\sigma^2_{qq}\right] = \left[\int_{-\infty}^{+\infty} \Phi_{qq}(\omega)\,d\omega\right] \tag{24}$$

The dependence on the gain matrix Q is now quadratic allowing for a straightforward convergence to a global optimal observer. It is worth noting that a matching between the observer introduced in Eq. (17) and the one defined by Eq. (13) can be achieved. Indeed, the zero-order observer can be obtained as the limit of the second-order observer presented in the previous section when the coefficients of L become large. Assuming that in a certain frequency range $||LS|| \gg ||H^{-1}||$ holds (see Eq. (12)), it yields:

$$H_0(\omega) \simeq (LS)^{-1}L \tag{25}$$

which is no more dependent on the frequency ω. Recalling Eq. (13) and taking into account Eq. (12), the proportional observer defined in Eq. (17) can be obtained as $Q = (LS)^{-1}L$. This implies that $QS = (LS)^{-1}LS = I$ and, thus, the error depends only on the measurement noise, *i.e.*,

$$\left[\sigma^2_{ee}\right] = Q\left[\sigma^2_{vv}\right]Q^{T}. \tag{26}$$

What is interesting here is that assuming $Q = (LS)^{-1}L$ allows us to cancel the contribution of the unknown inputs to the error and, consequently, a simple form of the error variance is obtained with Eq. (26). This may be an acceptable compromise only if $\left[\sigma^2_{vv}\right]$ is low, and this result is shared also by a second-order observer. Additionally, one has to pay attention to the condition that the square matrix (LS) must not be singular. As it will be clarified later, the latter relationship is exploited to assign the initial values for the optimization procedure aimed at obtaining the gain matrix L of the MBO.

3.2. Multi-Resolution Proportional Observer

The effectiveness of the presented PO technique can be improved by expressing the observer as a combination of proportional observers each one optimized for a specific element of a suitable signal decomposition of both the measurement and state-space vectors. Among the possible choice of signal decomposition, the wavelet multi-resolution analysis (WMRA) has been adopted (refer to Appendix A for more details). Let us first consider the following decomposition of the measurement vector into N_s functions spanning different time-scale ranges according to the WMRA:

$$y(t) = \sum_{n=1}^{N_s} y^{(n)}(t), \tag{27}$$

where the dependence on time is here highlighted for sake of clarity. By extending the PO definition in Eq. (23) for each time-scale function of the signal decomposition, one has:

$$\hat{q}^{(n)}(t) = Q_n y^{(n)}(t). \tag{28}$$

Thus, Eqs. (27) and (28) provide the following estimation of the generalized coordinates (see Fig. 1):

$$\hat{q} = \sum_{n=1}^{N_s} \hat{q}^{(n)} = \sum_{n=1}^{N_s} Q_n y^{(n)} \tag{29}$$

Therefore, defining $q^{(n)}$ as the n-th time-scale component of q obtained with the same signal decomposition (WMRA), it yields for the estimation error:

$$e = q - \hat{q} = \sum_{n=1}^{N_s} q^{(n)} - \sum_{n=1}^{N_s} \hat{q}^{(n)} = \sum_{n=1}^{N_s} \left(q^{(n)} - \hat{q}^{(n)}\right) = \sum_{n=1}^{N_s} e^{(n)} \tag{30}$$

In Eq. (30) the global error e depends on the errors at the different orders $e^{(n)}$, which have the following expression (see Eq. (18)):

$$e^{(n)} = (I - Q_n S)q^{(n)} - Q_n v^{(n)} \tag{31}$$

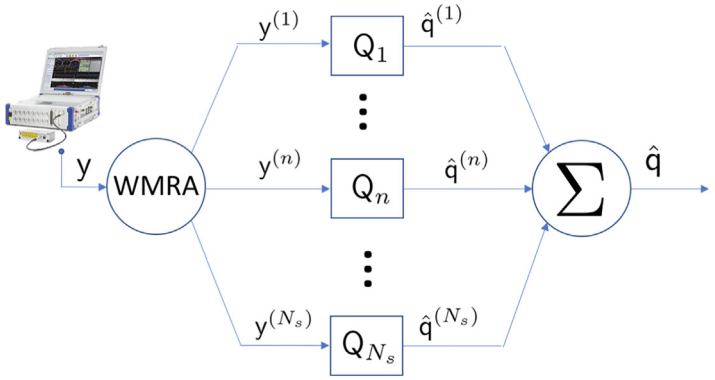

Fig. 1. MR-PO plant.

where the measurement noise is also decomposed into different contributions $v^{(n)}$ corresponding to the selected time scales. Next, using the properties of variance (Var) and covariance (Cov), one has:

$$\left[\sigma^2_{ee}\right] = \mathrm{Var}\left(\sum_{n=1}^{N_s} e^{(n)}\right) = \mathrm{Cov}\left(\sum_{n=1}^{N_s} e^{(n)}, \sum_{m=1}^{N_s} e^{(m)}\right) = \sum_{n=1}^{N_s}\sum_{m=1}^{N_s} \mathrm{Cov}\left(e^{(n)}, e^{(m)}\right) \tag{32}$$

which can be further recast as:

$$\left[\sigma^2_{ee}\right] = \sum_{n=1}^{N_s} \mathrm{Var}\left(e^{(n)}\right) + 2\sum_{n=1}^{N_s}\sum_{m=n+1}^{N_s} \mathrm{Cov}\left(e^{(n)}, e^{(m)}\right). \tag{33}$$

In a more coincise form, setting $\left[\sigma^2_{e,nm}\right] = \mathrm{Cov}\left(e^{(n)}, e^{(m)}\right)$, the previous equation can be expressed as:

$$\left[\sigma^2_{ee}\right] = \sum_{n=1}^{N_s} \left[\sigma^2_{e,mm}\right] + 2\sum_{n=1}^{N_s}\sum_{m=n+1}^{N_s} \left[\sigma^2_{e,nm}\right] \tag{34}$$

where, recalling Eq. (31), each matrix $\left[\sigma^2_{e,mm}\right]$ has the following expression:

$$\left[\sigma^2_{e,nm}\right] = (I - Q_n S)\left[\sigma^2_{q,nm}\right](I - Q_m S)^{\mathsf{T}} + Q_n \left[\sigma^2_{v,nm}\right] Q_m^{\mathsf{T}} \tag{35}$$

provided that the state-space vector q and the noise v are statistically independent, with $\left[\sigma^2_{q,nm}\right] = \mathrm{Cov}\left(q^{(n)}, q^{(m)}\right)$ and $\left[\sigma^2_{v,nm}\right] = \mathrm{Cov}\left(v^{(n)}, v^{(m)}\right)$. Though the covariance can be computed on the time-domain signals by definition, it is more efficient to carry out its evaluation in the frequency domain due to the linearity of the observed system. Therefore, by introducing the WMRA scalar transfer function $\tilde{\gamma}^{(n)}(\omega)$ associated to the n-th scale (see Appendix A), the Fourier transforms of the signals $q^{(n)}$ and $v^{(n)}$ can be obtained as:

$$\tilde{q}^{(n)}(\omega) = \tilde{\gamma}^{(n)}(\omega)\tilde{q}(\omega) \tag{36}$$

$$\tilde{v}^{(n)}(\omega) = \tilde{\gamma}^{(n)}(\omega)\tilde{v}(\omega). \tag{37}$$

Indeed, once specific wavelet and scaling functions are assigned, the WMRA based on orthogonal wavelets provides the related transfer functions $\tilde{\gamma}^{(n)}$. Therefore, the mixed-scale covariances associated to modal response and measurement noise, respectively, are given by:

$$\left[\sigma^2_{q,nm}\right] = \int_{-\infty}^{+\infty} \Phi_{qq,mn}\, d\omega = \int_{-\infty}^{+\infty} \tilde{\gamma}^{(n)}\tilde{\gamma}^{(m)}\, \Phi_{qq}\, d\omega \tag{38}$$

$$\left[\sigma^2_{v,nm}\right] = \int_{-\infty}^{+\infty} \Phi_{vv,mn}\, d\omega = \int_{-\infty}^{+\infty} \tilde{\gamma}^{(n)}\tilde{\gamma}^{(m)}\, \Phi_{vv}\, d\omega \tag{39}$$

where $\Phi_{qq,mn}(\omega)$ and $\Phi_{vv,mn}(\omega)$ are the cross-spectral densities relative to the components m and n of the considered signals, which are related to the PSD matrices $\Phi_{qq}(\omega)$ and $\Phi_{vv}(\omega)$, previously introduced for the PO (see Eqs. (21) and (22)). Eq. (34), along with Eq. (35) and the involved definitions by Eqs. (38) and (39), gives the objective function to be minimized for MR-PO. Because of the larger number of gain matrices Q_n with respect to the simpler PO approach, it is likely to improve the search for the minimum. However, it is worth noting that MR-PO maintains a quadratic form of the error covariance (see Eqs. (34) and (35)), despite involving a larger number of gain matrices.

4. Reference analytic case study

The above theory is applied to a slender beam with a two-side notch as shown in Fig. 2. The notch represents a feature that is not included in the equations of the observed system, *i.e.*, in Eq. (1). The Euler–Bernoulli equation of a beam lying on a spring layer is:

$$\frac{\partial^2}{\partial \bar{x}^2}\left[EI(\bar{x})\frac{\partial^2}{\partial \bar{x}^2}\left(\bar{w}+\eta_b\frac{\partial \bar{w}}{\partial \bar{t}}\right)\right]+k_s\left(\bar{w}+\eta_s\frac{\partial \bar{w}}{\partial \bar{t}}\right)+\mu(\bar{x})\frac{\partial^2 \bar{w}}{\partial \bar{x}^2}=\bar{p}(\bar{x}) \tag{40}$$

where $\bar{x}, \bar{t}$ and $\bar{w}$ are the dimensional abscissa, time and vertical displacement, respectively, $EI(\bar{x})$ and $\mu(\bar{x})$ are the piecewise constant sectional stiffness and mass, respectively, η_b is the structural damping coefficient, k_s and η_s are the spring and damping coefficients of the supporting elastic layer, respectively, and $\bar{p}$ is the external load expressed as force per unit length. The spring layer is added to represent a real structure on elastic foundations, floating condition or constrained for modal testing. The notch is represented with a reduction $\bar{b}_\delta$ of the width $\bar{b}$ of the rectangular section of the beam, while the height $\bar{h}$ is kept constant (see Fig. 2). Introducing a shape function $r_\delta(\bar{x})$, defined as $r_\delta=\bar{b}_\delta/\bar{b}$ along the notch, and equal to 1 elsewhere, width, sectional mass and stiffness ratio variations along the beam can be expressed in concise form.

It is convenient to recast Eq. (40) in non-dimensional form to generalize the considered case. By introducing a characteristic time t^*, a reference length l^* equal to the beam length l, and the sectional mass $\overline{\mu}$ and stiffness $\overline{EI}$ of the uniform beam, the following non-dimensional variables are defined:

$$x=\bar{x}/l \quad w=\bar{w}/l \quad t=\bar{t}/t^* \quad \kappa_b=\frac{\overline{EI}t^{*2}}{\overline{\mu}l^4} \tag{41}$$

$$\kappa_s=\frac{k_s t^{*2}}{\overline{\mu}} \quad \zeta_b=\eta_b/t^* \quad \zeta_s=\eta_s/t^* \quad p=\frac{\bar{p}t^{*2}}{\overline{\mu}l} \tag{42}$$

where t^* is the oscillating period of the first elastic mode of the uniform free-free beam without spring layer ($k_s=0$ and $r_\delta(\bar{x})=1$, the latter implying $EI(\bar{x})=\overline{EI}$ and $\mu(\bar{x})=\overline{\mu}$ in Eq. (40)). By substituting the above relationship into Eq. (40) and recalling that $EI(\bar{x})/\overline{EI}=\mu(\bar{x})/\overline{\mu}=r_\delta(\bar{x})$, one has:

$$\kappa_b\left[r_\delta(x)(w+\zeta_b\dot{w})''\right]''+\kappa_s(w+\zeta_s\dot{w})+r_\delta(x)\ddot{w}=p(x) \tag{43}$$

where the spatial derivative with respect to x is indicated with $'$ and the time derivative with respect to t with the dot $\dot{}$.

The Galerkin method is exploited to transform the partial differential equation above into a system of linear ordinary differential equations by decomposing the displacement $w(x,t)$ as a sum of modal contributions, *i.e.*, $w(x,t)\approx\sum_{n=1}^{N_{modes}}q_n(t)\psi_n(x)$, where the functions $\psi_n(x)$ are the analytical normal modes of the uniform undamped free-free beam without the spring layer ($r_\delta(\bar{x})=1$ and $\kappa_s=0$ in Eq. (43)), including the heave and pitch rigid-body modes (see Meirovitch, Ref. [25]). From the 'true' mass M_δ, (proportional) damping D_δ and stiffness matrices $\mathsf{K}_\delta=\mathsf{K}_\delta^{(b)}+\mathsf{K}^{(s)}$, by setting $r_\delta(\bar{x})=1$ the mass M, damping D and stiffness K matrices which define the structural model in Eq. (1) can be obtained. In this case, despite the presence of spring layer, the mass and stiffness matrices remain diagonal, and the rigid-body natural frequencies of the undamped system are analytically obtained as $\omega_1=\omega_2=\sqrt{\kappa_s}$.

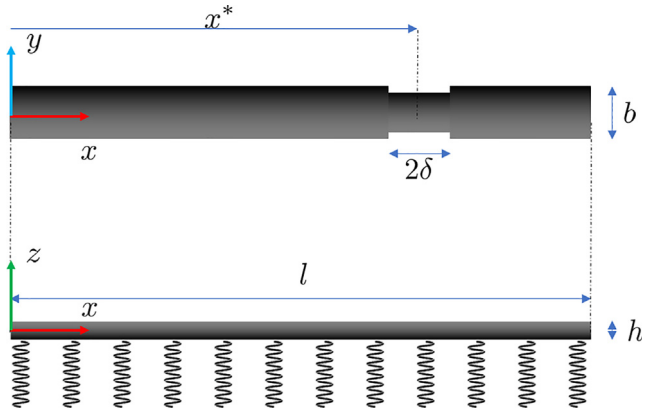

Fig. 2. Reference beam model.

An analytical expression of the process noise can be obtained as a mathematical model is available. By subtracting the equation of the beam with the notch from the equation of the uniform beam, one has:

$$n_w(x,t) = \kappa_b \frac{\partial^2}{\partial x^2}\left[r_\delta(\bar{x})\frac{\partial^2}{\partial x^2}(w+\zeta_b\dot{w})\right] + r_\delta(\bar{x})\ddot{w} \tag{44}$$

where, by definition, $n_w(x,t)$ is the process noise accounting for the presence of the notch as feature not considered in Eq. (1). By projection of Eq. (44) over the considered normal modes, one obtains the modal components $w_k(t)$ of the process noise vector $\mathrm{w} = \{w_1, w_2, \ldots, w_N\}^T$. Due to the linearity of the system, the process noise is likely to be described in the frequency domain. Setting $\tilde{\mathrm{w}}$ and $\tilde{\mathrm{f}}$ for the Fourier transformed modal components of process noise and load, one can obtain:

$$\tilde{\mathrm{w}} = \left(\mathrm{H}^{-1}\mathrm{H}_\delta - \mathrm{I}\right)\tilde{\mathrm{f}} \tag{45}$$

where H and H_δ are the FRF of the uniform and notched beams, respectively, with $\mathrm{H}_\delta(\omega) = \left[-\omega^2\mathrm{M}_\delta + i\omega\mathrm{D}_\delta + \mathrm{K}_\delta\right]^{-1}$.

5. Optimal gain computation

The numerical determination of the observer gain plays a central role in the estimation techniques presented in the previous sections. It implies finding the observer gain parameters depending on the considered technique (*i.e.*, L matrix for the MBO, Q matrix for the PO and several Q_n matrices for the MR-PO) which minimize the error variance defined by Eqs. (15), (23) and (33), respectively. Thus, the present section explains how the observer gain is numerically computed according to the different observer formulations (see Section 2 and 3). In Section 5.1 the definition of the corresponding optimization problems is discussed, and then in Section 5.2 the user inputs needed to start the optimization procedure are considered, namely, the power spectral densities of process and measurement noises as well as of external loads.

5.1. Optimization problem definition

Suitable optimization procedures are then employed for searching the optimum gain matrix and, consequently, different optimization problems are defined in terms of objective function, design variables and constraints, as resumed in Table 1.

All the optimization problems share the same objective function, which is the variance matrix $\left[\sigma^2_{\mathrm{ee}}\right]$ of the estimation error on the state-space vector q. The optimization problems for PO and MR-PO techniques are also similarly defined with differences related only to the presence of multiple terms related to the wavelet decomposition for the latter method, which requires a larger number of design variables (several Q_n instead of a single Q). The user input, as reported in Table 1, consists essentially in a statistical description of disturbances and noises, *i.e.*, the covariance matrix of the measurement noise and the PSD of process noise and external excitation. For both PO and MR-PO, a simple gradient-based algorithm as available in MATLAB© is employed for a full convergence to a global minimum since the objective function is quadratically dependent on the design variables. The optimizations are initialized with zero initial Q and Q_n matrices, such that at first step $\left[\sigma^2_{\mathrm{ee}}\right] = \left[\sigma^2_{\mathrm{qq}}\right]$.

On the other hand, MBO provides an objective function nonlinearly dependent on the gain L. At each evaluation of the objective function, it requires evaluating numerically the integral of Φ_{ee} over the frequency spectrum by suitable (unbounded) domain truncation. Indeed, the PSDs $\Phi_{\mathrm{ff}}(\omega), \Phi_{\mathrm{ww}}(\omega)$ and $\Phi_{\mathrm{vv}}(\omega)$ must be provided in place of their covariance matrices as user inputs. A constraint on the real part of the poles of $\mathrm{H}_e(\omega)$ (that has to be negative) is employed to ensure the stability of the observer. The nonlinear dependence on design variables (coefficients of the matrix L) makes the search of an optimum gain a more complex task than in the case of the PO-based methods. In this framework, proper initial values and a suitable optimization algorithm may positively affect the final values at the end of the optimization loop. In particular, in this work, both Gradient and Pattern Search algorithms available in MATLAB© have been tested to this end. Concerning the initial values for L, namely L_0, it is obtained by considering the similarity of the PO and MBO formulations for high values of L.

Table 1
Optimization statements for MBO, PO and MR-PO.

	MBO	PO	MR-PO
Objective	nonlinear $\left[\sigma^2_{\mathrm{ee}}\right]$ (see Eq. (15))	quadratic $\left[\sigma^2_{\mathrm{ee}}\right]$ (see Eq. (23))	quadratic $\left[\sigma^2_{\mathrm{ee}}\right]$ (see Eq. (33))
Design Variables	elements of L	elements of Q	elements of Q_n
Constraints	stability of $\mathrm{H}_e(\omega)$	none	none
Inputs	$\Phi_{\mathrm{ff}}(\omega), \Phi_{\mathrm{ww}}(\omega), \Phi_{\mathrm{vv}}(\omega)$	$\left[\sigma^2_{\mathrm{qq}}\right], \left[\sigma^2_{\mathrm{vv}}\right]$	$\left[\sigma^2_{\mathrm{q},nm}\right], \left[\sigma^2_{\mathrm{v},nm}\right]$
Algorithm	Gradient/ Pattern Search	Gradient	Gradient
Initial values	$(\mathrm{L}_0\mathrm{S})^{-1}\mathrm{L}_0 - \mathrm{Q} = \min_{\mathrm{L}_0}$	0	0

Once the observer gain Q of the PO is obtained, the initial values L_0 of the MBO, are evaluated by solving the following minimization problem (see Eq. (25)):

$$(L_0 S)^{-1} L_0 - Q = \min_{L_0}, \tag{46}$$

thus providing an error covariance evaluation at the first step in line with that expressed in Eq. (26). To ensure that at the end of the optimization process the minimum is locally 'strong', the solution for L is randomly perturbed and used as new initial condition for the optimization loop. If the new solution does not converge back to the initial condition, or the minimum for the objective function (in some metrics) is larger than the previous one, the gain L is perturbed again until the computed solution does not satisfy all the previous conditions.

5.2. Noise modeling

As mentioned above, the additional information required to evaluate the objective functions consist of some statistics on the measurement and process noises, as well as on the external forces, either directly provided by the covariance matrices or by the PSDs.

As far as it concerns the external forces, their PSD matrix $\Phi_{ff}(\omega)$ is generally derived by means of suitable spectral load models which depend on the statistical description of the environmental or operational excitation and on the transfer function from the excitation source (wind, waves, vibrations, etc) to the applied forces. In Section 6, PSDs of the external force are simply assigned, from which, one possible time dependent load distribution is derived. It is worth remarking that the same PSD assigned as input to build the observer is also used for modelling the response of mechanical system.

The measurement noise is modelled as white noise and featured by the signal-to-noise ratio (SNR) parameter, defined as it follows:

$$\mathrm{SNR} = \frac{\mathrm{tr}\left(\left[\sigma^2_{yy}\right]\right)}{\mathrm{tr}\left(\left[\sigma^2_{vv}\right]\right)} \tag{47}$$

The level of noise is equal for each virtual sensor and the PSD matrix is assumed diagonal, thus providing for a generic *k*-th sensor:

$$\Phi_{v_k v_k}(\omega) = \frac{\mathrm{tr}\left(\left[\sigma^2_{yy}\right]\right)}{M\,\omega_{max}\,SNR} \quad -\omega_{max}/2 < \omega < \omega_{max}/2 \tag{48}$$

where M is the number of sensors (later, the number of strain gages) and ω_{max} is the sampling frequency of the time histories.

Regarding the process noise accounting for structural imperfections, it has been already shown that Eq. (45) allows us to define it once the external forcing terms are assigned. This remark points out that the hypothesis of uncorrelated noises and forces is only approximately correct from a general point of view. On the other hand, in real-life applications using basic assumptions is mandatory. Apart from the aforementioned statistical independence, assumptions about structural uncertainties in terms of geometry or material properties are needed to set upper thresholds to unmodeled features. Thus, in this work, it is proposed to consider a 'white' process noise over the considered frequency range associated only to the diagonal terms of $\left[\sigma^2_{ww}\right]$, such that:

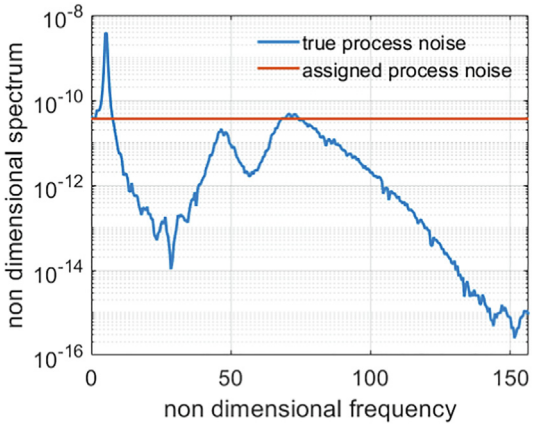

Fig. 3. Comparison between the modelled process noise and the one used to derive the observers. The blue line plots the process noise PSD for the first bending mode. (For interpretation of the references to colour in this figure legend, the reader is referred to the web version of this article.)

$$\Phi_{w_k w_k}(\omega) = \frac{\left[\sigma^2_{w_k w_k}\right]}{\omega_{max}} \quad -\omega_{max}/2 < \omega < \omega_{max}/2 \tag{49}$$

Figure 3 compares the constant PSD (white noise) provided as input in the calculations with the PSD of the diagonal element corresponding to the first vibration mode ($k = 3$), the latter provided by Eq. (45) once the PSD of the external forces has been assigned (see Section 6). The criterion here assumed for choosing the noise level is based on the equivalence in terms of signal power in the considered frequency range.

6. Numerical results

As stated in the previous sections, the present application aims at estimating the full field response based on pointwise measurements provided by strain gages in presence of an unknown excitation. In Section 6.1, the beam test-case outlined in Section 4 is further specified by assigning numerical values to the system parameters and the excitation function. In Section 6.2, the quantities related to the virtual measurement set-up (sensors and noise sources) are then characterized and the considered error metrics is defined as well. Finally, in Section 6.3 the analysis of the performance in estimating the system response is dealt with for the considered methods.

6.1. System parameters

The system parameters referring to the beam equation in non-dimensional form (see Eq. (43)) are reported in Table 2. With reference to Table 2, the non-dimensional modal frequencies of the uniform beam are computed and shown in Table 3, where five bending modes ($N_{modes} = 5$) are considered.

The load per unit length $p(x,t)$ is given by the sum of two terms, each one given by the product of a spatial shape function $\lambda_j(x)$ and a time dependent amplitude $p_{\lambda_j}(t)$, *i.e.*,

$$p(x,t) = p_{\lambda_1}(t)\lambda_1(x) + p_{\lambda_2}(t)\lambda_2(x) \tag{50}$$

where $\lambda_1(x) = e^{-\alpha_1 x}$ and $\lambda_2(x) = e^{\alpha_2(x-1)}$ are considered in this case study in order to have a distributed load with non-null projection over all the beam (bending) modes. The above functions $\lambda_j(x)$ are plotted in Fig. 4 for the values $\alpha_1 = \alpha_2 = 15$ used in the calculations. The modal forces can be obtained by projecting the function $p(x,t)$ on the eigenfunctions $\psi_k(x)$, thus expressing $p_k = C_{k1}p_{\lambda_1}(t) + C_{k2}p_{\lambda_2}(t)$, with the coefficients C_{kn} given as:

$$C_{kn} = \frac{\int_0^1 \lambda_n(x)\psi_k(x)\mathrm{d}x}{\int_0^1 |\psi_k(x)|^2 \mathrm{d}x} \tag{51}$$

To excite uniformly the system over a finite frequency interval, the time functions $p_{\lambda_1}(t)$ and $p_{\lambda_2}(t)$ are stochastic functions, whose power spectral densities $\Phi_{p_j}(\omega)$ (Fig. 5) follow a Gaussian distribution around a peak value $\omega_j^{(p)}$, *i.e.*,

$$\Phi_{p_j}(\omega) = \frac{A_j}{\bar{\sigma}_j\sqrt{2\pi}} e^{-\frac{\left(\omega-\omega_j^{(p)}\right)^2}{\bar{\sigma}_j^2}} + \frac{A_j}{\bar{\sigma}_j\sqrt{2\pi}} e^{-\frac{\left(\omega+\omega_j^{(p)}\right)^2}{\bar{\sigma}_j^2}} \tag{52}$$

with $\bar{\sigma}_j$ the standard deviation of the Gaussian distribution and $A_j = \sigma^2_{f_j}$ the variance of the random force components, shown in Table 4. A realization of the Gaussian process is shown in Fig. 6 where the load field along the beam is plotted with respect to time, which in turn determines the vertical displacement response of the uniform beam plotted in Fig. 7.

Table 2
Beam non-dimensional structural parameters.

Beam non-dimensional stiffness	κ_b	0.079
Spring non-dimensional stiffness	κ_s	1.579
Beam damping coefficient	ζ_b	0.002
Spring damping coefficient	ζ_s	0.2
Beam thickness	h	0.001

Table 3
Non-dimensional bending natural frequency of the uniform beam ($\delta = 0$).

rigid	heave	pitch	*bending modes*	2-nodes	3-nodes	4-nodes	5-nodes	6-nodes
$f = \bar{f}t^*$	0.20	0.20		1.02	2.77	5.41	8.94	13.35

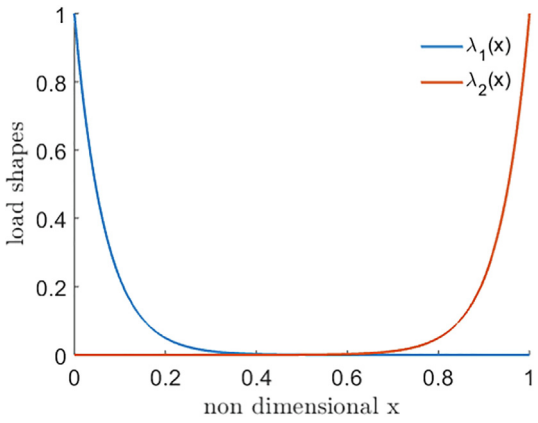

Fig. 4. Load shape functions $\lambda_1(x)$ and $\lambda_2(x)$.

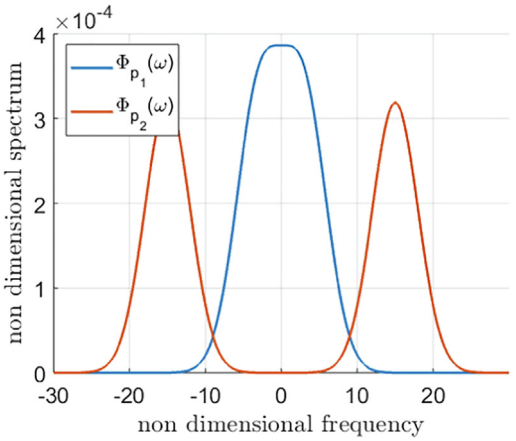

Fig. 5. Load spectra of the random functions $p_1(t)$ and $p_2(t)$.

Table 4
Gaussian spectrum parameters.

$\Phi_{p_j}(f)$	$A_j = \sigma_{f_j}^2$	$\omega_j^{(p)}$	$f_j^{(p)}$	$\bar{\sigma}_j$
Φ_{p_1}	0.002	18.84	3.00	3.00
Φ_{p_2}	0.002	94.20	15.00	3.00

The analyses are carried out by using MATLAB ©. The simulations have a non-dimensional sampling frequency equal to 60. The wavelet multi-resolution analysis is performed within the embedded wavelet toolbox using Daubechies dB12 orthogonal wavelets (Ref. [26]). Specifically, $N_s = 4$ time scales are considered for the present analyses. The corresponding WMRA scalar transfer functions $\gamma_k(\omega)$ are illustrated in Fig. 8 highlighting their frequency content.

6.2. Displacement field estimation

In the present application, the measurement set consists of noisy data relative to the strains on the top face of the beam at equidistant positions. The reconstruction of the elastic displacement field is done via the estimation of the modal coordinates $\hat{q}_j$ according to the following decomposition of the response:

$$\hat{w}(x,t) = \sum_{k=3}^{N_{modes}} \hat{q}_k(t)\psi_k(x), \tag{53}$$

with $\psi_k(x)$ the vertical bending modes of the uniform structure, since the rigid-body modes (heave and pitch) do not generate strain response. For the sake of clarity, in the following we will refer only to the bending modes by renumbering

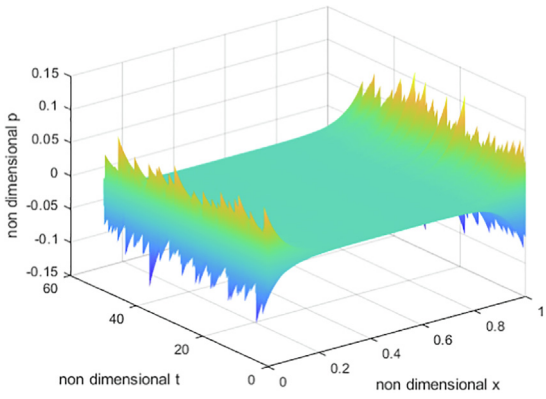

Fig. 6. Time-history of the load distribution along the beam.

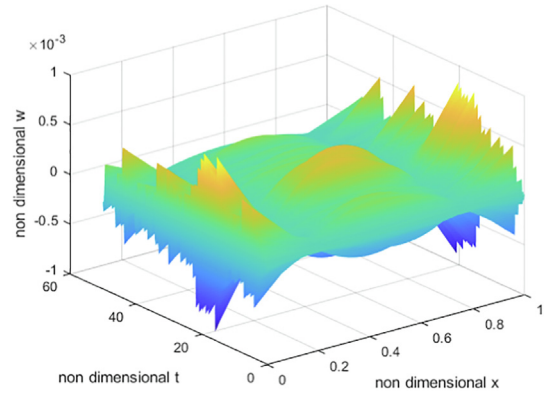

Fig. 7. Displacement response of the beam under load history depicted in Fig. 6.

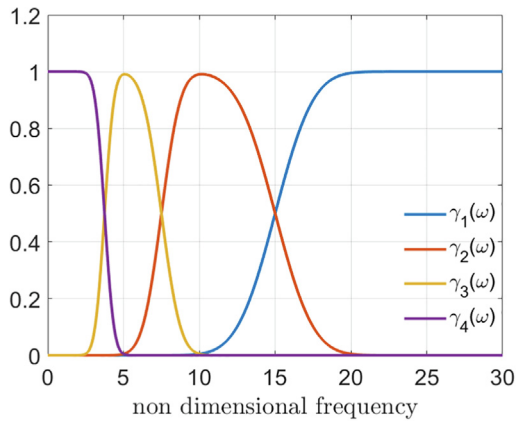

Fig. 8. WMRA scalar transfer functions for the considered test case.

the bending modes or the corresponding modal coordinates from $n = 1$ to $n = 5$. To assess the accuracy of each technique, different estimations of the modal coordinate $\hat{q}_j(t)$ are compared to each other and to the true solution $q_j(t)$. In the following, this comparison is carried out mainly in terms of a frequency representation of the error relative to the estimation of the modal coordinates as provided by their analytical form in Eq. (15). As the predictions are affected by modelling and measurement uncertainties as well as by the number $M = N_{sg}$ of experimental dofs at sensor locations, the corresponding values are set in Table 5 where a reference case is defined. In the considered reference case, the number of strain sensors N_{sg} is equal to 4. Since $M = N_{sg} \neq N_{modes} = N$, most of the involved matrices are rectangular as it is likely to occur in real-life applications.

Table 5
Baseline non-dimensional parameters.

Number of strain gages	N_{sg}	4
Signal-to-Noise Ratio	SNR	20
Position of damage	x^*	0.7
Length of notch	$2\,\delta$	0.1
Percentage reduction of transverse section	r_δ	95%

Moreover, setting $N_{sg} < N_{modes}$ makes the estimation process more challenging than assuming $N_{sg} > N_{modes}$. Each strain-gage is supposed to be glued on the top side of the beam at the generic position $x_k^{(sg)}$ providing the virtual measurement of the strain ε_{xx} along the x direction. The strain of the k-th sensor will be referred as ε_k for the sake of conciseness. Thus, the N_{sg} elements y_k of the measurement output are provided by strains as:

$$y_k(t) = \varepsilon_k + v_k(t), \tag{54}$$

where the functions $v_k(t)$ indicating the measurement noise differ only for the phase but not for their statistical content. Considering the relation between the strain and the vertical beam displacement in the linear case (small displacements), it follows:

$$y_k(t) = \frac{h}{2}\frac{\partial^2 w(x,t)}{\partial x^2}\bigg|_{x=x_k^{(sg)}} + v_k(t), \tag{55}$$

being $h/2$ the distance between the strain sensor and the neutral axis.

The sensitivity analysis of the estimations will concern the variation of one or two of these parameters at the same time as it will be clear later. Corresponding to the reference case in Table 5, the variance matrices of the measurement and process noises used in the error evaluation are reported below:

$$[\sigma_{vv}^2] = \mathrm{diag}([0.375 \quad 0.375 \quad 0.375 \quad 0.375])$$
$$[\sigma_{ww}^2] = 10^{-7}\mathrm{diag}([0.911 \quad 0.321 \quad 0.021 \quad 0.040 \quad 0.081])$$

These matrices, whose dimensions depend on the number of sensors ($N_{sg} = 4$) and on the number of modes involved ($N_{modes} = 5$), respectively, will change as long as noise levels are varied. The effect of the notch depth on the beam response accounted by r_δ can be quantitatively evaluated by considering the modal displacement response with respect to the load input $p(x,t) = p_{\lambda_1}(t)\lambda_1(x)$ with zero initial conditions. For this purpose, the following ratios are defined for each component of the state-space vector:

$$R_k(\omega) = \frac{\tilde{q}_k(\omega)}{\tilde{p}_{\lambda_1}(\omega)}, \tag{56}$$

where the functions $R_k(\omega)$ are computed and plotted in Fig. 9 for $k = 1, \ldots, 4$. It is worth noting that the modulus of the frequency response for the generic p mode is altered at the resonant frequencies corresponding to the $k < p$ modes.

The fidelity level of the observation process is addressed by means of the so called *Time Response Assurance Criterium* (TRAC) (see Ref. [4]). By taking into account the generalized coordinate vector $\mathrm{q}(t)$ and its estimation $\hat{\mathrm{q}}(t)$, the TRAC is defined as below:

$$\mathrm{TRAC}(t) = \frac{\|\mathrm{q}(t)^{\mathsf{T}}\hat{\mathrm{q}}(t)\|^2}{\left(\mathrm{q}(t)^{\mathsf{T}}\mathrm{q}(t)\right)\left(\hat{\mathrm{q}}(t)^{\mathsf{T}}\hat{\mathrm{q}}(t)\right)}. \tag{57}$$

The function above represents the similarity of the signals vectors q and $\hat{\mathrm{q}}$ in time domain and can assume values between 0 (when orthogonal) and 1 (when parallel). This property makes the TRAC a good candidate for being considered as a quality indicator of the estimation process. Its time-averaged value $\overline{\mathrm{TRAC}}$ is therefore assumed as a global indicator for the quality of the estimation.

6.3. Results

The first analysis considers an ideal case, *i.e.*, the beam without the notch with negligible noise on the measurements ($SNR = 100$), virtually equipped with as many strain-gages as the number of modes, *i.e.*, $N_{sg} = N_{modes}$. This case considers no modelling errors and faultless measurements for displacement field reconstruction and, consequently, the order of magnitude of the error keeps globally rather small as shown via $\overline{\mathrm{TRAC}}$ in Fig. 10(f) (orange bars). The PO (yellow line) and MBO (blue line) show very close results for the low-order modes (see Figs. 10(b)). For $n \geqslant 3$, the PO is less accurate around the natural frequency of the considered mode (recall that the first bending mode now corresponds to $n = 1$ and so on). However, it tends to perform better than the MBO elsewhere. The MR-PO gives in general better results than PO and MBO in all the

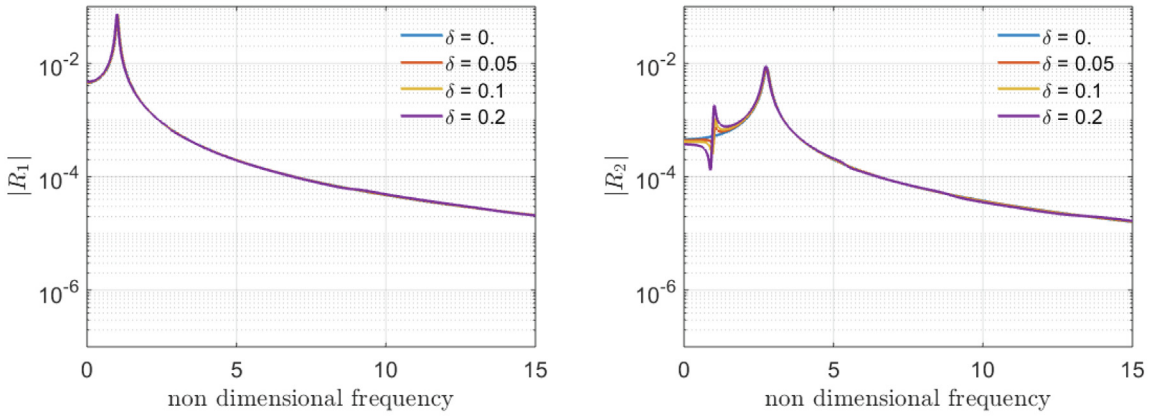

(a) Mode 1. (b) Mode 2.

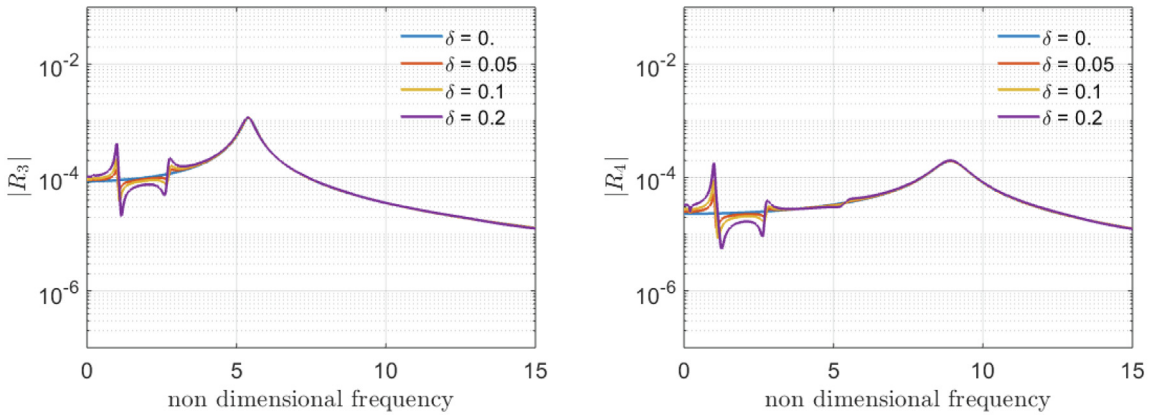

(c) Mode 3. (d) Mode 4.

Fig. 9. Absolute value of frequency response functions $R_k(\omega)$ to load 1 for different value of notch depth.

frequency range, making errors to reduce further far from the mode natural frequency thanks to the signal decomposition. The ability of finding an optimal gain matrix affects all the results but becomes critical for the MBO technique, where iterations may stop once a local minimum is identified. In Figs. 10(e) a curve representing the error done at first iteration by MBO using the initial guess of the gain matrix according to Eq. (46) is shown as a red line labelled as MBO-i (MBO single iteration). At first iteration, a sharp error peak appears at low frequency for most modes corresponding to the excitation frequency spectrum. This peak is then strongly reduced as the optimization iterations proceed up to the final value, indicating that the optimization procedure is effective. Also in terms of global error, the red bar in Fig. 10(f) indicates that the TRAC at first iteration gives poor results with respect to the full-developed MBO computation.

If the signal-to-noise ratio is decreased to 20 (see Fig. 11), errors grow for all the considered techniques (see $\overline{\text{TRAC}}$ in Fig. 11(f)). Some differences among the involved techniques, already present in the case of low-noise, are amplified, like the error increase around resonances for the PO technique as shown in Figs. 10(e). Nonetheless, for $n \geqslant 3$ MBO seems to suffer more the higher measurement noise. It is worth noting that MR-PO keeps the modal error at the same level of the case with SNR $= 100$ far from the natural frequencies of each mode.

Next, the number of sensors is decreased to 4 and the corresponding results are shown in Fig. 12 and 13. Whatsoever the value of the SNR, errors again decrease as the mode order is increased. At SNR $= 100$, the various techniques perform in a similar way to the case with $N_{sg} = 5$ at least for $n = 1, 2, 4$, keeping approximately the same accuracy. For the odd modes ($n = 3, 5$) the error distribution in frequency, especially for the MBO, exhibits greater variations with an overall significant decrease in its accuracy. Similar considerations about the comparison between using 4 or 5 sensors apply also if SNR is set to 20 as shown in Fig. 13.

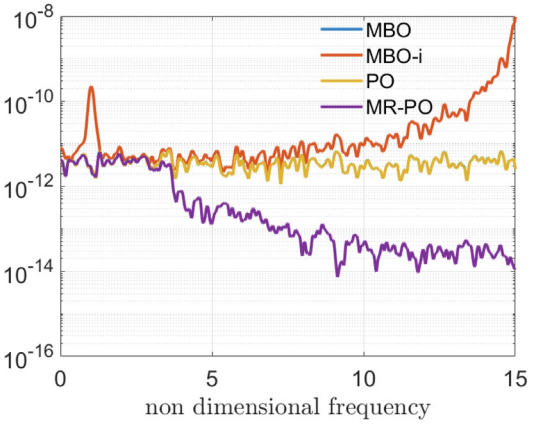

(a) mode 1.

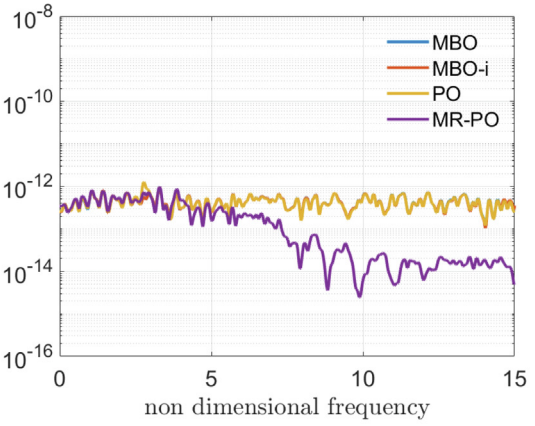

(b) mode 2.

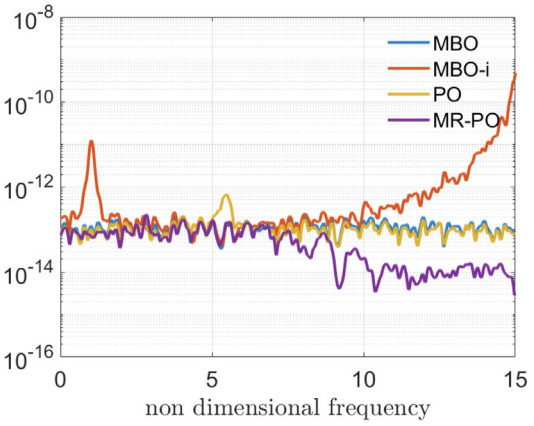

(c) mode 3.

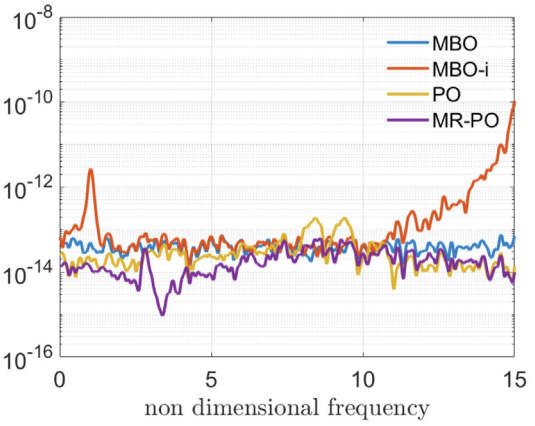

(d) mode 4.

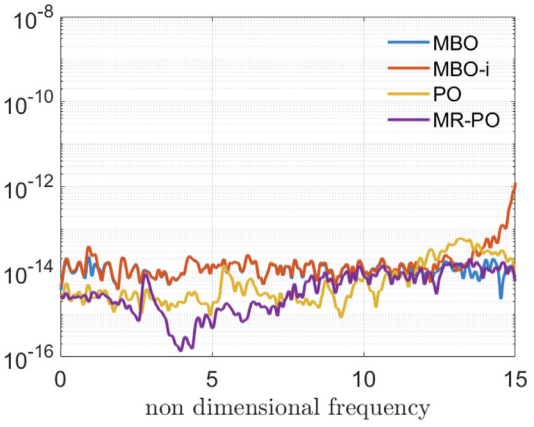

(e) mode 5.

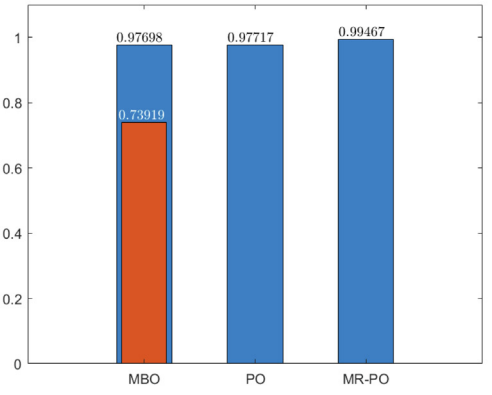

(f) $\overline{\text{TRAC}}$.

Fig. 10. Power spectral density amplitude for all the modal coordinates (a-e) and $\overline{\text{TRAC}}$ (f) for the case $N_{sg} = N_{modes} = 5, SNR = 100$, uniform beam (no notch).

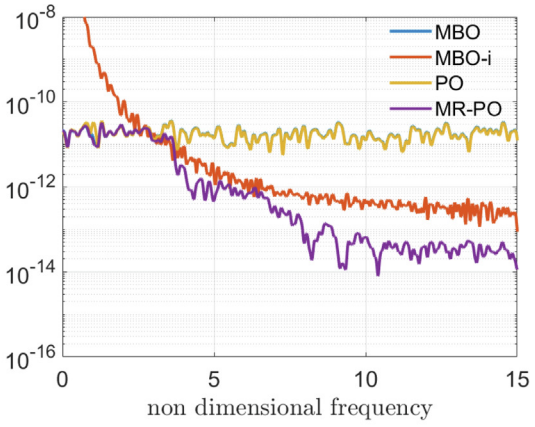

(a) mode 1.

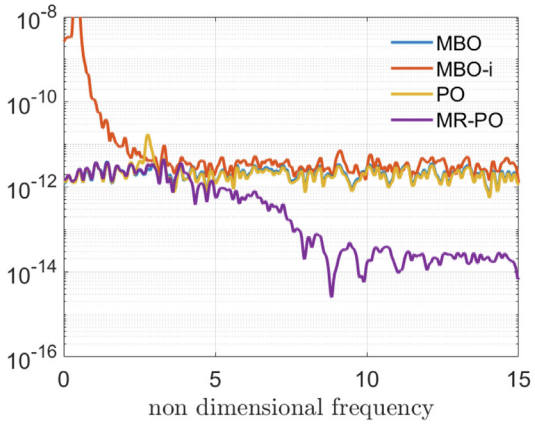

(b) mode 2.

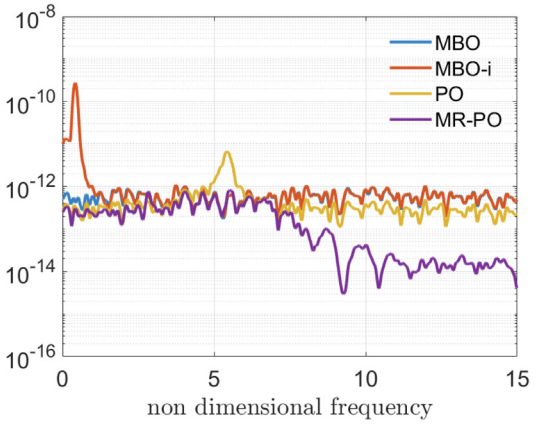

(c) mode 3.

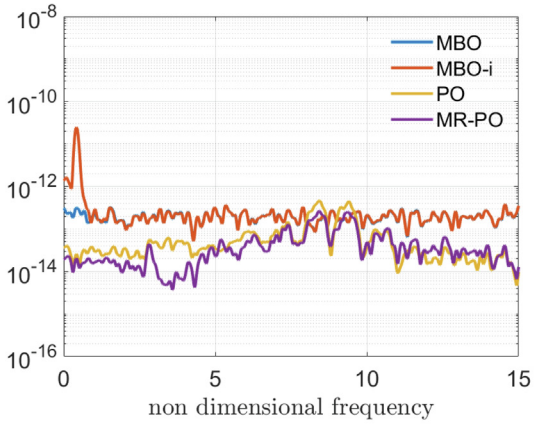

(d) mode 4.

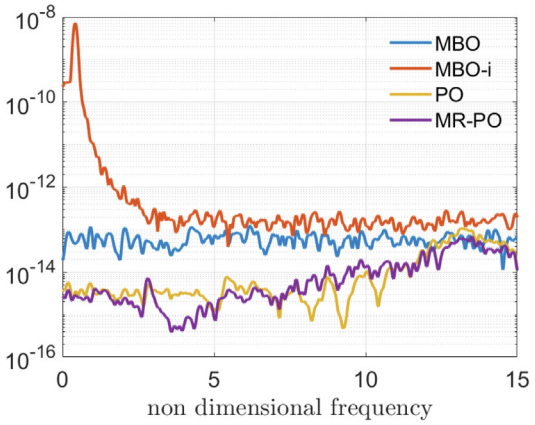

(e) mode 5.

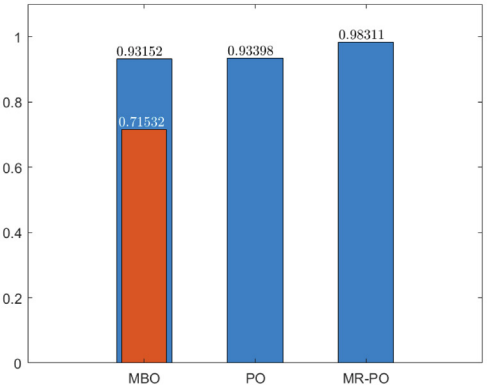

(f) $\overline{\text{TRAC}}$.

Fig. 11. Power spectral density amplitude for all the modal coordinates (a-e) and $\overline{\text{TRAC}}$ (f) for the case $N_{sg} = N_{modes} = 5, \text{SNR} = 20$, uniform beam (no notch).

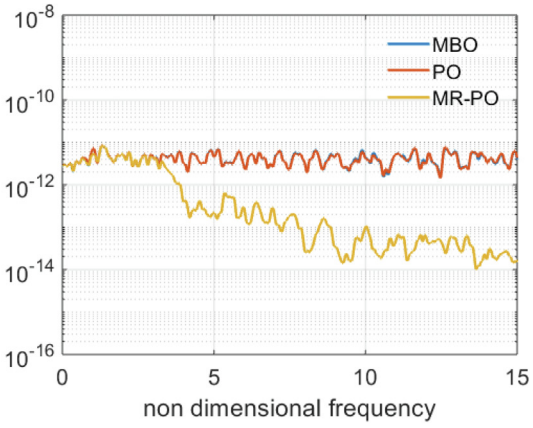

(a) mode 1.

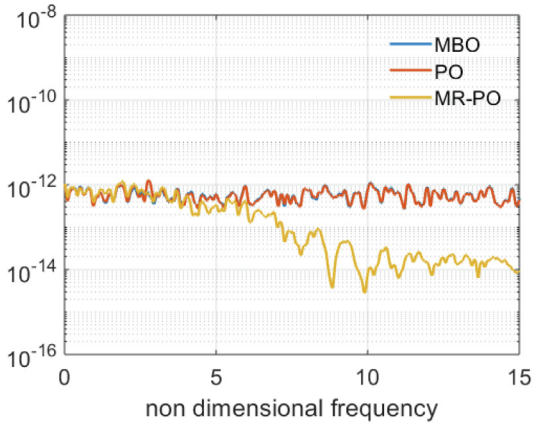

(b) mode 2.

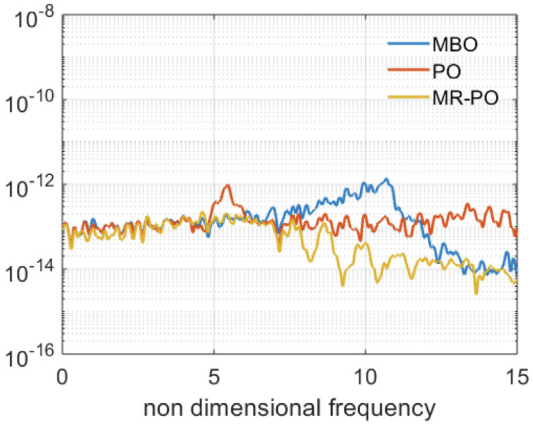

(c) mode 3.

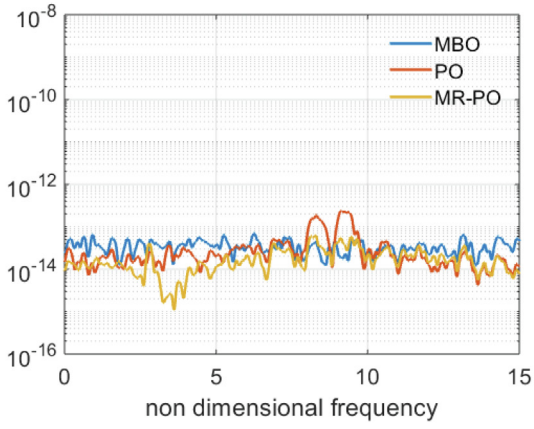

(d) mode 4.

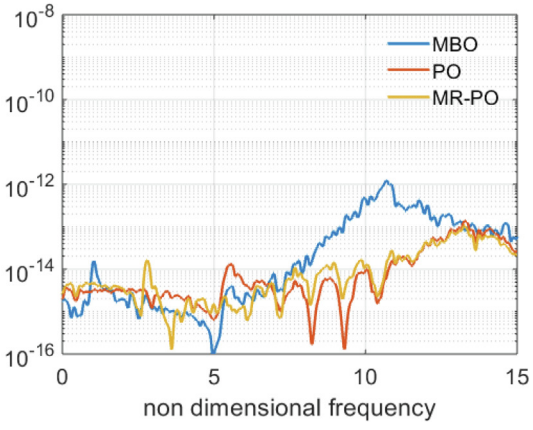

(e) mode 5.

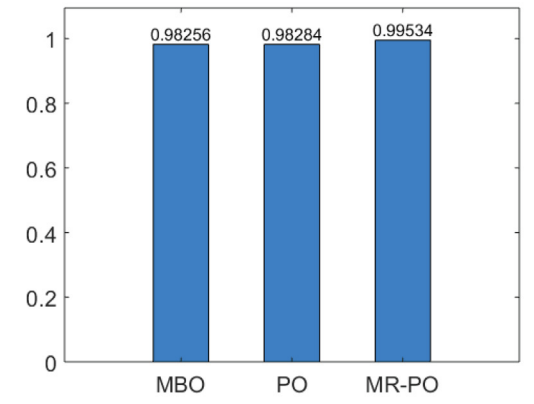

(f) $\overline{\text{TRAC}}$.

Fig. 12. Power spectral density amplitude for all the modal coordinates (a-e) and $\overline{\text{TRAC}}$ (f) for the case $N_{sg} = 4, \text{SNR} = 100$, uniform beam (no notch).

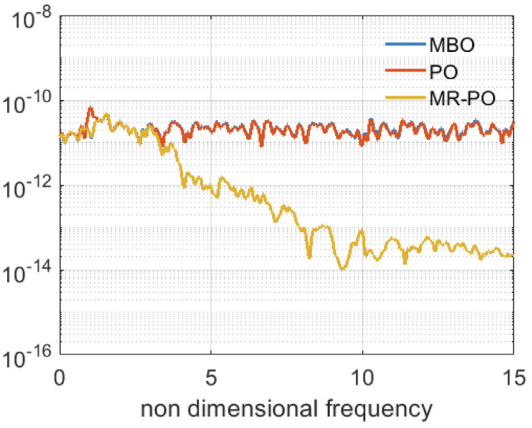

(a) mode 1.

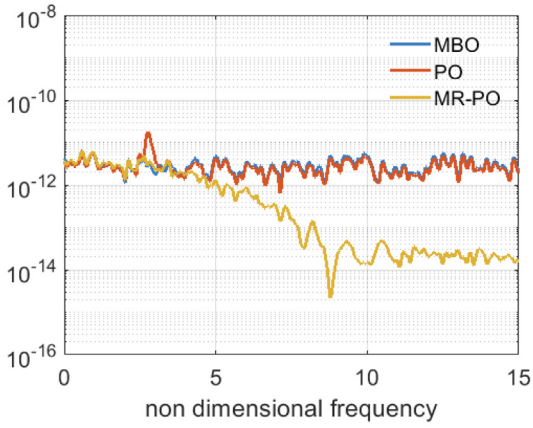

(b) mode 2.

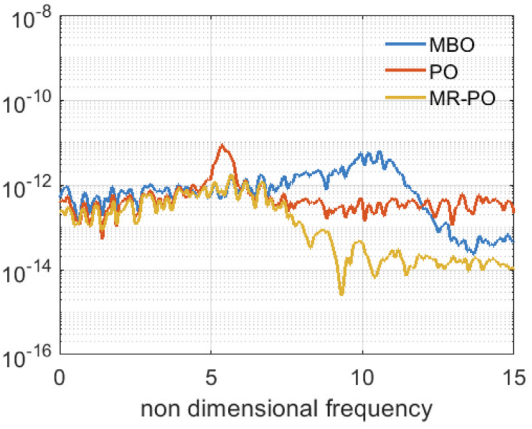

(c) mode 3.

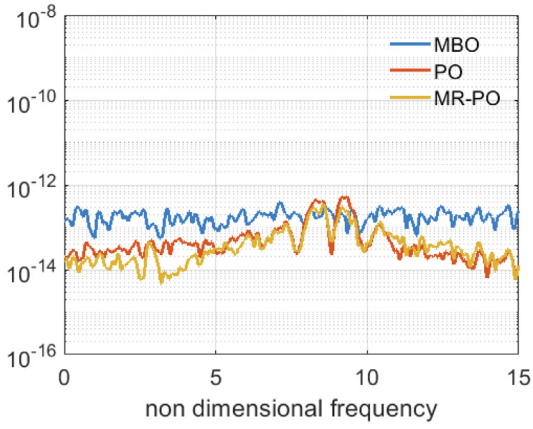

(d) mode 4.

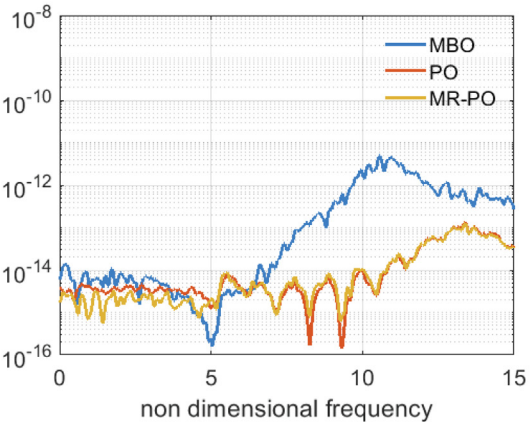

(e) mode 5.

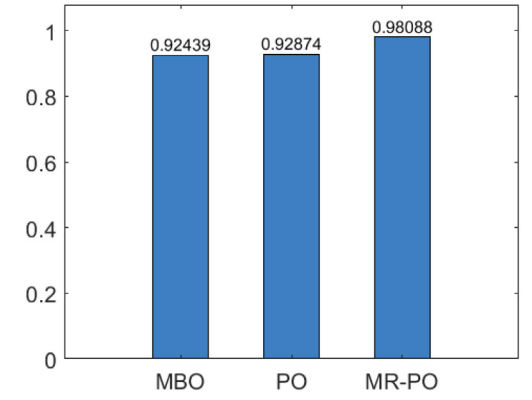

(f) $\overline{\text{TRAC}}$.

Fig. 13. Power spectral density amplitude for all the modal coordinates (a-e) and $\overline{\text{TRAC}}$ (f) for the case $N_{sg} = 4, \text{SNR} = 20$, uniform beam (no notch).

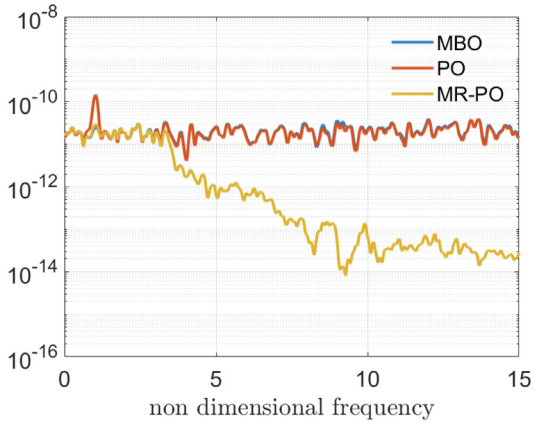

(a) mode 1.

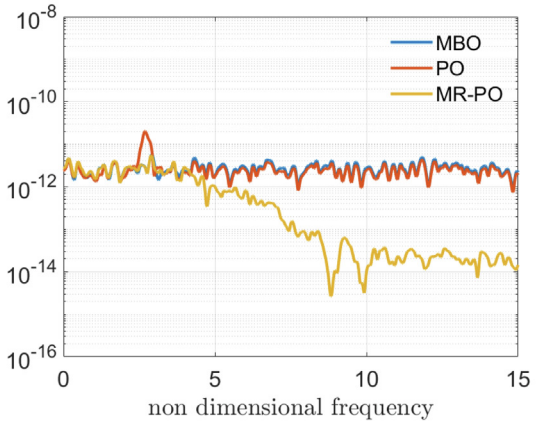

(b) mode 2.

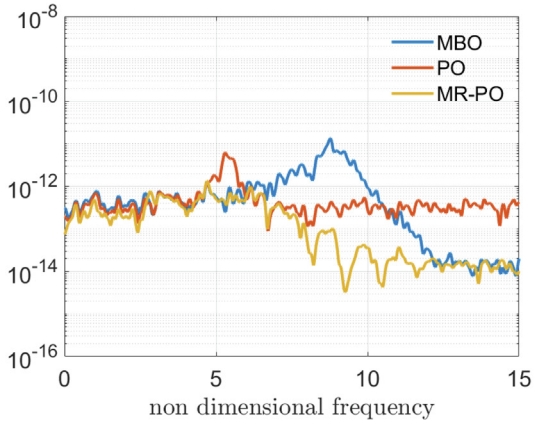

(c) mode 3.

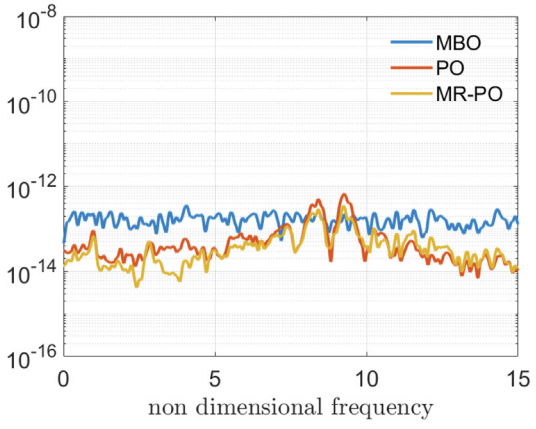

(d) mode 4.

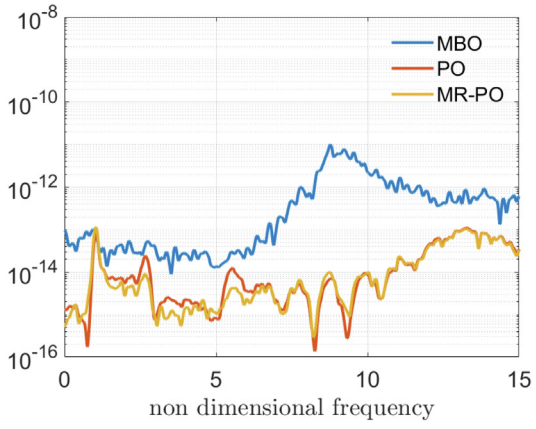

(e) mode 5.

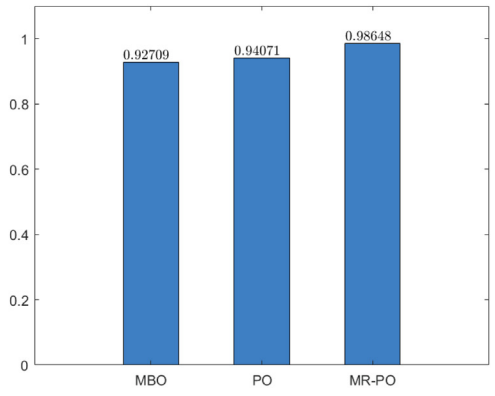

(f) $\overline{\text{TRAC}}$.

Fig. 14. Power spectral density amplitude for all the modal coordinates (a-e) and $\overline{\text{TRAC}}$ (f) for the case with baseline parameters (see Table 5).

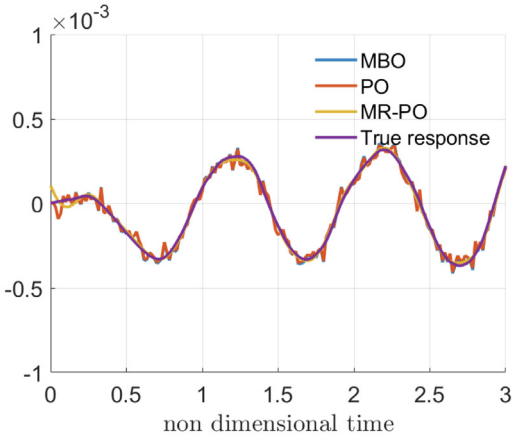

(a) mode 1.

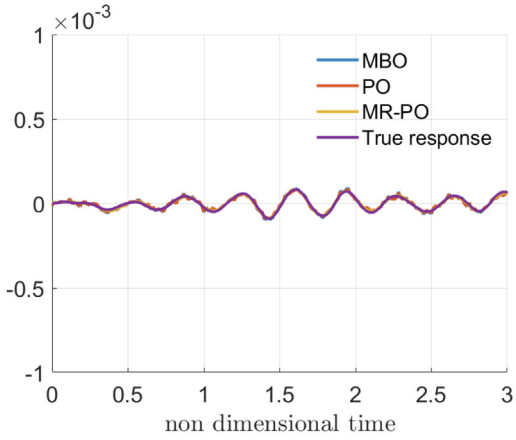

(b) mode 2.

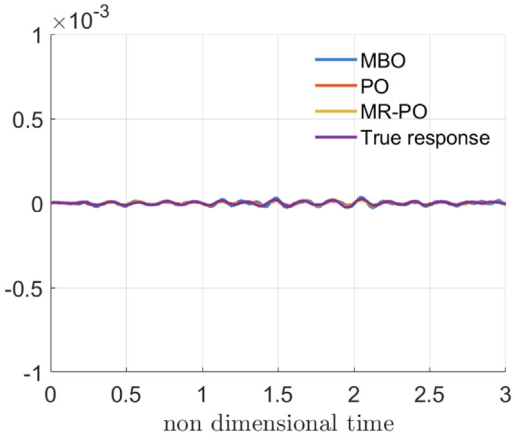

(c) mode 3.

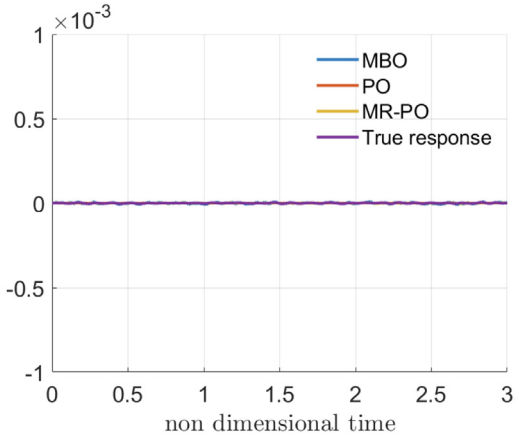

(d) mode 4.

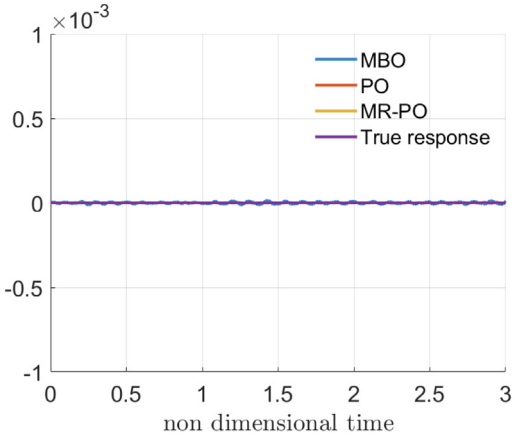

(e) mode 5.

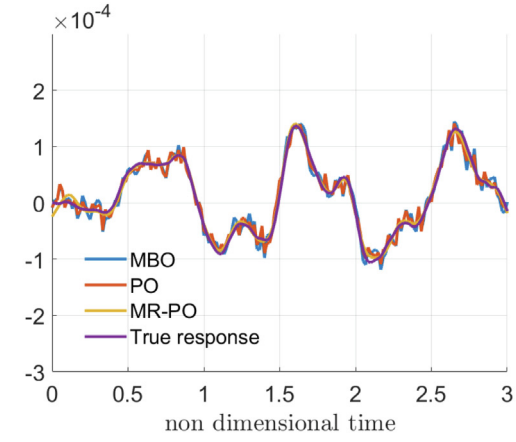

(f) $\hat{w}(x = 0.7, t)$

Fig. 15. Modal response (a-e) and reconstructed vertical displacement in $x = 0.7$ (f) for the reference case (see Table 5).

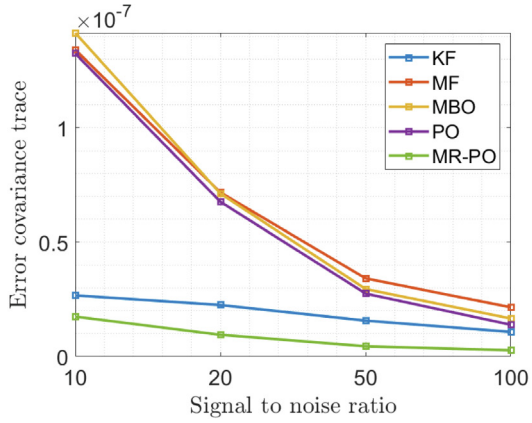

(a) Error covariance matrix sensitivity to SNR.

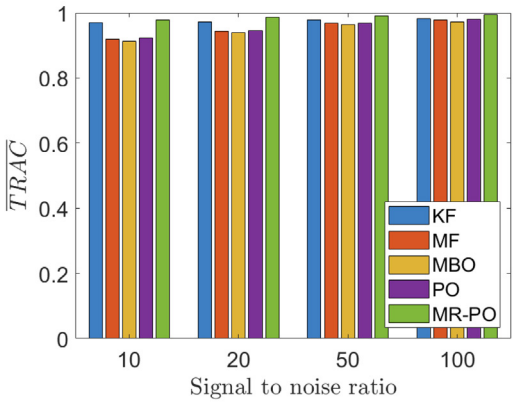

(b) $\overline{\text{TRAC}}$ sensitivity to SNR.

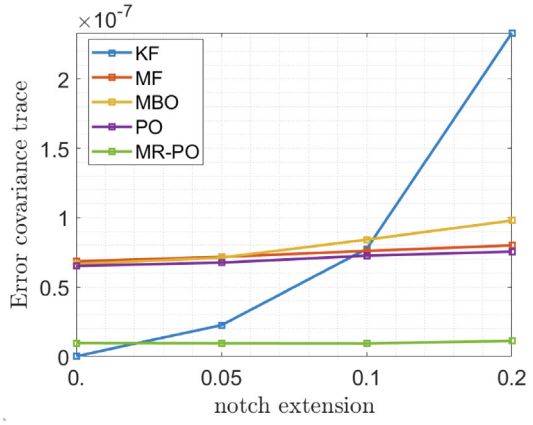

(c) Error covariance matrix sensitivity to notch depth.

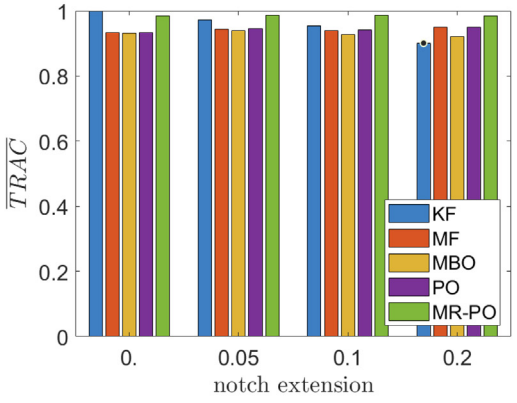

(d) $\overline{\text{TRAC}}$ sensitivity to notch depth.

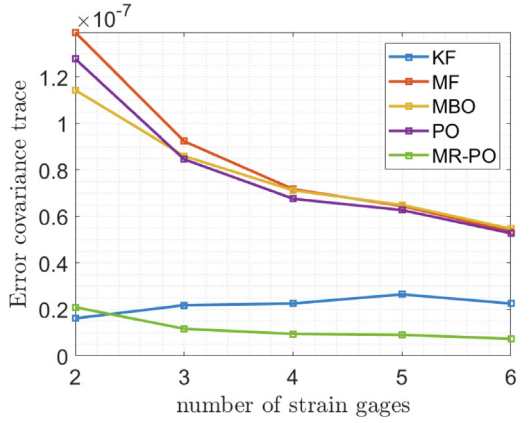

(e) Error covariance matrix sensitivity to N_{sg}.

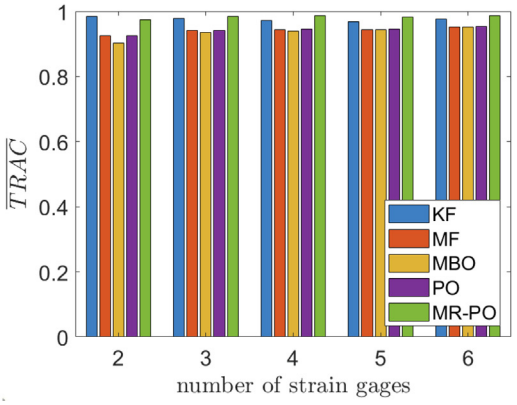

(f) $\overline{\text{TRAC}}$ sensitivity to N_{sg}.

Fig. 16. Sensitivity of the trace of the error covariance matrix and $\overline{\text{TRAC}}$ with respect signal-to-noise ratio, nothc depth and number of strain gauges.

In the following, the so-called reference case of Table 5 is analyzed; the beam geometry is modified by adding a stiffness reduction (refer to Fig. 2) representing a structural detail that is not *a priori* known due to its relatively small extension. In this case, the error distribution among all the techniques and modes remains substantially the same (see Fig. 14) For this baseline configuration, the estimation of structural responses in time domain is shown in Figs. 15(a) and 15(e) in terms of modal response and vertical displacement of the point coinciding with the notch position (centred around $x = 0.7$) in Fig. 15(f), each compared with the true solution. It is noted that the estimate of MR-PO is substantially close to the true solution and is less sensitive to the presence of noise as compared to MBO and PO.

However, though less reasonable in real applications, it is interesting to understand in which way the notch dimensions will affect the accuracy of results. A sensitivity analysis with respect to the relative width reduction as described by the parameter $(b - b_\delta)/b = 1 - r_\delta$ is first carried out. Later, the sensitivity analysis is extended to cope also with the measurement noise, given by the signal-to-noise ratio SNR, and the number of strain gages N_{sg}. The parameters are then varied starting from the reference case (Table 5). The trace of the error covariance matrix $\mathrm{Tr}\left[\sigma^2_{qq}\right]$ and the $\overline{\mathrm{TRAC}}$ indexes are assumed as key performance indicators for the comparison. For the sake of completeness, also the results relative to the Kalman filter (KF) and Modal filter (MF) (see Meirovitch (1985), Ref. [6]) have been added. It is worth highlighting that KF benefits from requiring, as input, the time-dependent loads acting on the beam. On the other hand MF is performed by projecting the vibration modes over deflection field obtained by integrating piece-wise linear function of w'' between sensors and beam edges (equivalent to natural spline approximation). The error (left) and the accuracy (right) sensitivity to different values of the SNR are plotted in Figs. 16(a) and 16(b), respectively. For all the techniques, there is a general monotonic increase of the error as the SNR grows. As expected, less information. *i.e.*, a smaller number of sensors, affects the quality of the results. It is also worth to note that for $N_{sg} = 2$ the PO makes an error larger than MBO. Indeed, it is likely to occur that the MBO takes advantage of using more knowledge about the system model than the PO in the definition of the observer. Anyway, the MR-PO still provides the best results among all the considered techniques. Varying the notch depth, *i.e.*, the process noise, the nonlinearity of the optimization search of the best gain becomes evident for the MBO technique. For PO and MR-PO the sensitivity with respect to the process noise is less evident; this is related to the fact that these techniques rely to a minor extent on the knowledge of the system model.

7. Conclusions

In this paper, the problem of reconstructing the vertical displacement field over a beam using point-wise measurements has been addressed as a specific but meaningful example of virtual sensing for building a digital twin based on experimental data. The so-called Multi-Resolution Proportional Observer has been proposed as a generalization of the Proportional Observer, introduced in the paper as well, to follow closely the different components of the tracked signals according to the signal decomposition given by wavelet multi-resolution analysis. A detailed mathematical derivation of both the techniques (PO and MR-PO) highlights similarity and differences with the MBO approach which shares the same objective to be a 'natural' observer. The displacement field reconstruction is then based on a modal superposition, where the mode shapes are obtained from the numerical model of the mechanical system (mass, damping and stiffness matrices) and the time coordinates are estimated by the observer.

Though the final goal is developing numerical techniques for processing real experimental data, *i.e.*, sensor signals, in the present paper the focus has been on providing a comprehensive error analysis with reference to a 'virtual' experiment, which allows for achieving a deeper insight into the performances of the proposed methods. Thus, all the noise sources like measurement noise, unknown excitation, and process noise, have been taken into account by their statistical behavior (power spectral densities), properly specified for the considered application. The capability of accurately reconstructing the whole displacement field relies on choosing the global observer gain, in the form of a set of gain matrices, which minimizes the variance matrix of the error between the true and the estimated state-space vector. This minimization process is carried out directly on the analytic expression of the error variance matrix which depends on the observer parameters. From a general point of view, it would be possible to avoid the evaluation analytical expressions of the error variance matrix as provided in the paper. Indeed, in real cases one may divide the set of sensors into measurement and control sensors, the latter not providing any information as input but just the reference values which the predicted values are compared with. Though recalling that the error estimation based on its analytic expression depends on the model uncertainties as well, the present procedure has some advantages: (*i*) it highlights clearly the type of error dependence from the observer gain matrix, that is found to be quadratic for the PO observers at the considered time-scales so facilitating the search for an absolute minimum, and (*ii*) it is numerically more efficient in terms of the error computation at each iteration of the optimization process.

Remaining on the field of highlighting the applicability of these methods to real cases, theoretical or empirical statistical models for the unknown load and noise sources are required. For instance, if environmental loads due to stochastic gust on wing airplanes, or random waves on ship hulls are considered, the parameters characterizing the correspondent spectral models can be identified by means of local forecast or inferred from on-board measurement. Then, a linear transfer function from the excitation source (*e.g.*, flow velocity for wings or wave elevation for ships) to the applied forces is needed as well as to obtain the final input load spectra. A similar user expertise applies to the modelling of structural uncertainties. If structural damage or degradation is the reason of an unmodeled feature, it is reasonable to assume that the severity of the stiffness reduction should be below a certain detection threshold, depending on the considered problem. It is reasonable

indeed to assume that evident structural modifications would be included by the user when addressing the virtual sensing problem.

The error sensitivity has been carried out with respect to increasing levels of both the measurement and process noise, as well as with respect to the number of virtual strain-gages so highlighting the best performances in all the conditions for the MR-PO. This is in general true considering both the global error, evaluated with the average of TRAC function, or its frequency spectrum. The displacement error, evaluated in specific points along the beam, is then the results of the error in estimating the modal time coordinates, the error in computing the mode shapes, and the interpolation error directly related to the modal truncation. The results appear rather encouraging on extending this method to the case of experimental measurements on more complex structures for which the development of these approaches finds its ultimate motivation.

Declaration of Competing Interest

The authors declare that they have no known competing financial interests or personal relationships that could have appeared to influence the work reported in this paper.

CRediT authorship contribution statement

Francesco Saltari: Methodology, Software, Writing - original draft, Writing - review & editing. **Daniele Dessi:** Methodology, Writing - original draft, Writing - review & editing. **Franco Mastroddi:** Methodology, Writing - original draft, Writing - review & editing.

Appendix A. Wavelet multi-resolution analysis

The aim of this appendix is to provide the basic elements to understand the wavelet multi-resolution analysis as applied to the definition of the proposed observer (for further details, the reader is addressed to Ref. [26,27]). The wavelet multi-resolution analysis (WMRA) expresses a signal $s(t)$ into different contributions, each one related to different time scales, by performing a cascade of dicothomic decompostions, which at the generic n-level generate a detail $d_n(t)$ and an approximation signal $a_n(t)$. While the detail $d_n(t)$ is kept as a component of the signal $s(t)$, the approximation $a_n(t)$ is further decomposed at the $(n+1)$-level into a new approximation $a_{n+1}(t)$ and a new detail $d_{n+1}(t)$. After N decompositions, this cascade process yields:

$$s(t) = a_N(t) + \sum_{n=1}^{N} d_n(t), \tag{A.1}$$

where $a_N(t)$ is the (residual) approximation at N-th level and the summation includes N details $d_n(t)$. In the framework of WMRA, the approximation $a_n(t)$ can be generally expressed as:

$$a_n(t) = \sum_{k=-\infty}^{\infty} \alpha_{n,k} \phi\left(2^{-n}t - k\right) \tag{A.2}$$

where $\phi\left(2^{-n}t - k\right)$ is the so called k-th scaling function, with $k \in \mathbb{Z}$, forming a set of orthogonal functions spanning the subspace $\mathscr{V}_{-n}$. The scaling function satisfies the following relationship (the so-called *refinement equation*):

$$\phi\left(2^{-n-1}t\right) = \sum_{k=-\infty}^{\infty} h(k) \phi\left(2^{-n}t - k\right) \tag{A.3}$$

which guarantees that the subspace $\mathscr{V}_{-n-1}$ is completely spanned by the basis functions $\phi\left(2^{-n}t - k\right)$ of $\mathscr{V}_{-n}$, implying $\ldots \mathscr{V}_{-n-1} \subset \mathscr{V}_{-n} \subset \mathscr{V}_{-n+1} \ldots$. Consequently, a proper subspace $\mathscr{W}$ can be introduced to represent the difference between consecutive spaces, *e.g.*, $\mathscr{V}_{-n-1}$ and $\mathscr{V}_{-n}$:

$$\mathscr{V}_{-n-1} = \mathscr{V}_{-n} \oplus \mathscr{W}_{-n}. \tag{A.4}$$

In the same way, recalling Eq. (A.2), the approximation function $a_n \in \mathscr{V}_{-n-1}$ can be expressed in terms of the approximation at higher order $a_{n+1} \in \mathscr{V}_{-n}$ plus a correction term lying in the subspace $\mathscr{W}_{-n}$, *i.e.*,

$$a_n(t) = a_{n+1}(t) + \sum_{k=-\infty}^{\infty} \beta_{n+1,k} \psi\left(2^{-n-1}t - k\right) \tag{A.5}$$

where $\psi(t)$ is the so called mother wavelet function that in the wavelet multi-resolution framework satisfies an equation similar to that one which holds for the scaling equation (cfr. Eq. (A.3)):

$$\psi\left(2^{-n-1}t\right) = \sum_{k=-\infty}^{\infty} g(k) \phi\left(2^{-n}t - k\right). \tag{A.6}$$

The discrete wavelet transform (DTW) coefficients $\alpha_{n,k}$ and $\beta_{n,k}$ are then defined as the components of the signal $s(t)$ over the scaling and mother wavelet functions, respectively:

$$\alpha_{n,k} = \int_0^\infty s(t)\phi*\left(2^{-n}t-k\right)\mathrm{d}t, \quad \beta_{n,k} = \int_0^\infty s(t)\psi*\left(2^{-n}t-k\right)\mathrm{d}t, \tag{A.7}$$

where $*$ denotes complex conjugate. The coefficients $h(k)$ and $g(k)$ represent a conjugate pair of a mirror filter based on the scaling and mother wavelet functions:

$$h(k) = \int_0^\infty \phi(t)\phi^*(2t-k)\mathrm{d}t, \quad g(k) = \int_0^\infty \psi(t)\phi^*(2t-k)\mathrm{d}t \tag{A.8}$$

which implies $g(k) = (-1)^k h(-k+1+2n)$. The decomposition in Eq. (A.1) is computationally achieved by means of the Mallat algorithm that employs the conjugate filter pair defined in Eq. (A.8) (Ref. [27]) alternate with the down-sampling of the coefficients in Eq. (A.7). Fig. A.17(a) illustrates graphically a decomposition tree over 3 levels. The sampled signal $s(t_k)$ is first decomposed by means of the digital filter pair in the approximation $a_1(t)$ and detail $d_1(t)$ functions (first level), and then down-sampled (with decimation factor equal to 2). This procedure is recursively applied to the approximations until the desired N-level is reached, thus providing a cost-effective strategy to compute the discrete wavelet coefficients. The obtained DTW coefficients are then used to compute the approximation a_N and details d_n as represented in Fig. A.17(b). The bottom side of the figure highlights the frequency-range overlapping of each detail and approximation components.

In the development of the multi-resolution proportional observer (MR-PO) the previous definitions and analysis tools are employed using problem-oriented notations. Given the number of scales N_s for the WMRA in Section 3.2, the generic component $q_n(t)$ of the state-space vector is decomposed into a set of functions $q_1^{(1)} \dots q_1^{(N_s-1)}$, which represent the details function, and the function $q_1^{(N_s)}$ that is the 'approximation'. This applies for all the other variables as well. Several transfer functions $\tilde{\gamma}^{(n)}(\omega)$ relating the decomposition sub-signals $\tilde{s}^{(n)}(t)$ to the target signal $\tilde{s}(t)$ in frequency domain are also introduced. These transfer functions $\tilde{\gamma}^{(n)}(\omega)$ are obtained *a posteriori* with respect to the wavelet analysis and depend on the kind of orthogonal wavelet used for the decomposition. In this work, the use of these functions represent an effective method for the evaluation of the cross time-scales covariances employed to compute the optimal Q_n (see Eq. (38)).

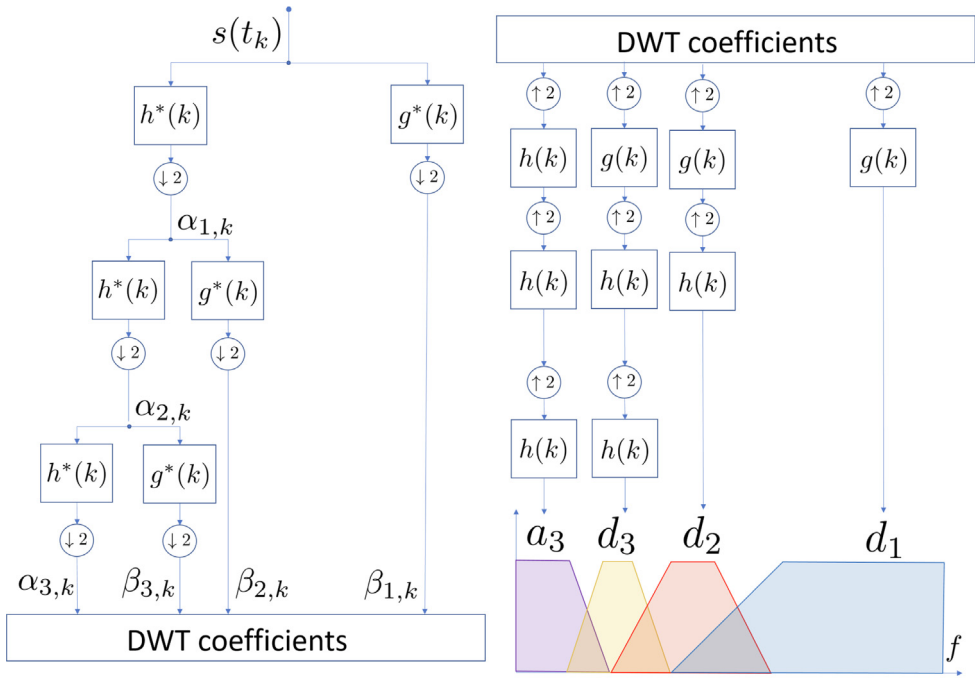

(a) Decomposition. (b) Reconstruction.

Fig. A.17. 3-level WMRA decomposition and reconstruction diagrams.

References

[1] A. Maniatty, N. Zabaras, K. Stelson, Finite element analysis of some inverse elasticity problems, J. Eng. Mech. 115 (6) (1989) 1303–1317.
[2] S. Shkarayev, R. Krashantisa, A. Tessler, An inverse interpolation method utilizing in-flight strain measurements for determining loads and structural response of aerospace vehicles, Proc. Third Int. Workshop on Structural Health Monitoring, Stanford, California,, 2001, pp. 336–343.
[3] A. Tessler, J.L. Spangler, A least-squares variational method for full-field reconstruction of elastic deformations in shear-deformable plates and shells, Comput. Methods Appl. Mech. Eng. 194 (2–5) (2005) 327–339.
[4] P. Avitabile, P. Pingle, Prediction of full field dynamic strain from limited sets of measured data, Shock Vibr. 19 (2012) 765–785.
[5] J. Kullaa, Virtual sensing of structural vibrations using dynamic substructuring, Mech. Syst. Signal Process. 79 (2016) 203–224.
[6] L. Meirovitch, H. Baruh, Implementation of Modal Filters for control of structures, J. Guid. Control Dyn. 8 (1985) 707–716.
[7] G.C. Smith, R.L. Clark, A crude method of loop-shaping adaptive structures through optimum spatial compensator design, J. Sound Vib. 247 (3) (2001) 489–508.
[8] P.M. Suh, A.W. Chin, D.N. Mavris, Virtual Deformation Control of the X-56A Model with Simulated Fiber Optic Sensors, in: AIAA Atmospheric Flight Mechanics (AFM) Conference, Boston, Massachusetts, 2013.
[9] J. Hwang, A. Kareemb, W. Kim, Estimation of modal loads using structural response, J. Sound Vib. 326 (2009) 522–539.
[10] C. Papadimitriou, C.P. Fritzen, P. Kraemer, E. Ntotsios, Fatigue predictions in entire body of metallic structures from a limited number of vibration sensors using Kalman filtering, Struct. Control Health Monit. 18 (2011) 554–573.
[11] E. Lourens, E. Reynders, G. De Roeck, G. Degrande, G. Lombaert, An augmented Kalman filter for force identification in structural dynamics, Mech. Syst. Signal Process. 27 (2012) 446–460.
[12] S. Gillijns, B. De Moor, Unbiased minimum-variance input and state estimation for linear discrete-time systems with direct feedthrough, Automatica 43 (2007) 934–937.
[13] E. Lourens, C. Papadimitriou, S. Gillijns, E. Reynders, G. De Roeck, G. Lombaert, Joint input-response estimation for structural systems based on reduced-order models and vibration data from a limited number of sensors, Mech. Syst. Signal Process. 29 (2012) 310–327.
[14] F. Naets, J. Croes, W. Desmet, An online coupled state/input/parameter estimation approach for structural dynamics, Comput. Methods Appl. Mech. Eng. 283 (2015) 1167–1188.
[15] M.J. Balas, Do all linear flexible structures have convergent second-order observer?, in: Proceedings of the American Control Conference, Philadelphia, Pennsylvania, 1998
[16] H.R. Hashemipour, A.J. Laub, Kalman filtering for second-order models, J. Guidance, Control, Dyn. 11 (2) (1988) 181–186.
[17] W.K. Belvin, Second-order state estimation experiments using acceleration measurements, J. Guid., Control, Dyn. 17 (1) (1994).
[18] M.A. Demetriou, Natural second-order observers for second-order distributed parameter systems, Syst. Control Lett. 51 (2004) 225–234.
[19] M.A. Demetriou, Using unknown input observer for robust adaptive fault detection in vector second-order systems, Mech. Syst. Signal Process. 19 (2005) 291–309.
[20] M.M. Azad, J. Mohammadpour, K.M. Grigoriadis, Observer-type H_∞ filter design for structural systems, in: AIAA Guidance, Navigation and Control Conference and Exhibit, Honolulu, Hawaii, 2008.
[21] E.M. Hernandez, A natural observer for optimal state estimation in second order linear structural systems, Mech. Syst. Signal Process. 25 (2011) 2938–2947.
[22] E.M. Hernandez, Optimal model-based state estimation in mechanical and structural systems, Struct. Control Health Monit. 20 (2013) 532–543.
[23] K. Erazo, E.M. Hernandez, A model-based observer for state and stress estimation in structural and mechanical systems: Experimental validation, Mech. Syst. Signal Process 43 (2014) 141–152.
[24] F. Saltari, D. Dessi, E. Faiella, F. Mastroddi, Load and deflection estimation of a fast catamaran towing-tank model via reduced order modeling and optimal natural observer, Proceedings of ISMA 2018 – International Conference on Noise and Vibration Engineering and USD 2018 – International Conference on Uncertainty in Structural Dynamics, Leuven, Belgium,, 2018, p. 3495.
[25] L. Meirovitch, Elements of Vibration Analysis, McGraw-Hill, 1975.
[26] I. Daubechies, Ten lectures on Wavelets. CBMS-NSF Regional Conference Series in Applied Mathematics, 1992.
[27] S.G. Mallat, G. Zhang, Matching pursuits with time-frequency dictionaries. IEEE Trans. Signal Process., **41**, 3397–3415.